Atmos. Meas. Tech. Discuss., 4, 3401–3497, 2011
www.atmos-meas-tech-discuss.net/4/3401/2011/
doi:10.5194/amtd-4-3401-2011

Atmospheric
Measurement
Techniques
Discussions

Progress in turbulence detection via GNSS occultation data

L. B. Cornman[1], R. K. Goodrich[1,2], P. Axelrad[2], and E. Barlow[2]

[1]National Center for Atmospheric Research, Boulder, USA
[2]University of Colorado, Boulder, USA

Received: 1 March 2011 – Accepted: 10 March 2011 – Published: 1 June 2011

Correspondence to: L. B. Cornman (cornman@ucar.edu)

Published by Copernicus Publications on behalf of the European Geosciences Union.

Abstract

The increased availability of radio occultation (RO) data offers the ability to detect and study turbulence in the Earth's atmosphere. An analysis of how RO data can be used to determine the strength and location of turbulent regions is presented. This includes the derivation of a model for the power spectrum of the log-amplitude and phase fluctuations of the permittivity (or index of refraction) field. The bulk of the paper is then concerned with the estimation of the model parameters. Parameter estimators are introduced and some of their statistical properties are studied. These estimators are then applied to simulated log-amplitude RO signals. This includes the analysis of global statistics derived from a large number of realizations, as well as case studies that illustrate various specific aspects of the problem. Improvements to the basic estimation methods are discussed, and their beneficial properties are illustrated. The estimation techniques are then applied to real occultation data. Only two cases are presented, but they illustrate some of the salient features inherent in real data.

1 Introduction

There is a long and distinguished history in the study of electromagnetic (EM) wave propagation through random media (cf. Tatarskii, 1971; Yeh and Liu, 1982; Ishimaru, 1997). These works have provided a firm theoretical foundation for estimating statistical properties of the neutral atmosphere and ionosphere via the statistical properties of the received EM signals. That is, the characteristics of the turbulent atmosphere can be deduced from, for example, correlation and/or spectral analysis of the phase and/or amplitude of the received signal. In the past, the bulk of the experimental analysis in this area has been performed with ground-based transmitters and receivers (e.g., radars and lidars), as well as with ground-based receivers and space-based transmitters. With the advent of Global Navigation Satellite System (GNSS) constellations, a new avenue has become available to investigate the turbulence properties of the earth's atmosphere. The deployment of an ever-increasing number of Low Earth Orbiting (LEO) satellites – with high quality, high-sampling rate receivers – provides a very valuable new source of turbulence measurements: GNSS-LEO occultations.

Previous efforts to study turbulence in the upper troposphere, stratosphere and ionosphere with GNSS occultations fall into a two broad categories: ones that applied appropriate wave propagation theory to data analysis, simulation, and ones that used limited, or occasionally, inappropriate techniques based on the relevant theory. In the former category, most of those analyses were of a case-study nature, whereas in the latter category there have been numerous case studies and a few larger-scale studies. Furthermore, the bulk of the previous efforts have been focused on the study of the ionosphere. A few studies have been performed to investigate gravity waves and turbulence in the stratosphere. On the other hand, very few works have addressed the characterization of turbulence in the upper troposphere and lower stratosphere.

There are numerous other practical applications which can benefit by having turbulence measurements (and resultant climatologies) from GNSS-aircraft occultations. For example: space weather (Hajj et al., 2000), transionospheric communication links (Secan et al., 1997), aviation safety and navigation systems (Cornman et al., 2004; Conker et al., 2003), the accuracy of ground-based GNSS receivers (Ganguly, 2004), as well as the effect of turbulence on measuring atmospheric state variables from GNSS-LEO occultations (Gorbunov and Kirchengast, 2005).

In this paper, a detailed analysis of the problem is presented, including the derivation of a model for the power spectrum of the log-amplitude and phase fluctuations of the permittivity (or index of refraction) field. The bulk of the paper is then concerned with the estimation of model parameters, such as the intensity and location of the turbulence along the line of sight. A thorough study of the properties of the parameter estimators is presented using simulated data. This includes global statistics over a large number of realizations, as well as case studies that illustrate various specific aspects of the problem. The application of the methodologies is then made with real occultation data.

Only two cases are presented, but they illustrate some of the salient features inherent in real data.

2 Wave propagation theory

If polarization effects can be ignored, the vector wave equation for monochromatic signals, derived from Maxwell's equations can be written in the scalar form,

$$\left(\nabla^2 + k^2\,\varepsilon\,(\boldsymbol{r})\right)\,U(\boldsymbol{r}) \;=\; 0 \tag{1}$$

where U is a component of the electric field (a transverse component for our case), k is the (constant) wavenumber for the transmitted frequency, $k = 2\pi f/c = 2\pi/\lambda$, and ε is the permittivity of the medium. The index of refraction, n, is given by $\varepsilon = n^2$, and free space is characterized by $\varepsilon = 1$. In deriving Eq. (1), it has been assumed that the temporal dependence is $e^{-i\varpi t}$. Equation (1) is known as the Helmholtz equation. In order to solve this equation in a unique form, boundary conditions and the so-called Sommerfeld radiation conditions must also be imposed. The radiation condition is needed to insure causality, i.e., since the Helmholtz equation is quadratic in derivatives, there are two valid solutions, one that describes outgoing waves and one that describes incoming waves. The radiation condition forces the solution to be associated with the out-going wave solution, as well as dying off at infinity.

The Helmholtz equation is a seemingly benign equation, but in fact encompasses an extremely wide variety of wave propagation problems. In this work, the focus is on characterizing the statistical properties of the permittivity based upon measurements of the electric field, i.e., this is an inverse problem. A formal solution of Eq. (1) can be constructed as follows. Re-write Eq. (1) as

$$\left(\nabla^2 + k^2\right)\,U(\boldsymbol{r}) \;=\; -k^2\,\varepsilon'(\boldsymbol{r})\,U(\boldsymbol{r}) \tag{2}$$

where $\varepsilon = 1 + \varepsilon'$. The associated Green's function for this problem is defined by

$$\left(\nabla^2 + k^2\right) G\left(\boldsymbol{r} - \boldsymbol{r}'\right) = -\delta\left(\boldsymbol{r} - \boldsymbol{r}'\right) \tag{3}$$

Multiplying Eq. (2) by $G(\boldsymbol{r}-\boldsymbol{r}')$ and Eq. (3) by $U(\boldsymbol{r}')$, subtracting and then integrating over $\boldsymbol{r}'$ gives

$$\int \left[G\left(\nabla^2 + k^2\right) U - U\left(\nabla^2 + k^2\right) G\right] d\boldsymbol{r}' \tag{4}$$

where we have dropped the explicit reference to position for clarity of notation. Using $\nabla^2 U = -k^2 \varepsilon' U$ and $\nabla^2 G = -\delta$ gives

$$U(\boldsymbol{r}) = \int \left[G\, \nabla^2 U - U\, \nabla^2 G\right] d\boldsymbol{r}' + k^2 \int G\, \varepsilon'\, U\, d\boldsymbol{r}' \tag{5}$$

In order to ensure existence of the second integral on the right-hand side, it is assumed that the inhomogeneous parts of the permittivity have compact support. The first integral on the right-hand side contains the information regarding boundary conditions. This can be seen by applying Green's Theorem to convert the integral over the volume into an integral over the surface of the volume. Since we do not know a priori the value of G and U on the surface, it is typical to assume a form of U inside the boundary. For example, if we assume that $U = U_0$ (the incoming – or free-space wave, which is the solution to the homogeneous wave equation, $(\nabla^2 + k^2)\, U_0\,(\boldsymbol{r}) = 0$), then the first integral on the right-hand side of Eq. (5) becomes

$$\int \left(G\, \nabla^2 U_0 - U_0\, \nabla^2 G\right) d\boldsymbol{r}' = U_0\left(\boldsymbol{r}\right) \tag{6}$$

Plugging this into Eq. (5) gives the so-called Lippmann-Schwinger integral equation,

$$U(\boldsymbol{r}) \approx U_0\left(\boldsymbol{r}\right) + k^2 \int G(\boldsymbol{r} - \boldsymbol{r}')\, \varepsilon'(\boldsymbol{r}')\, U(\boldsymbol{r}')\, d\boldsymbol{r}' \tag{7}$$

This says that the electric field component at the point $\boldsymbol{r}$ is given by the incoming field plus a "scattering" term due to the inhomogeneities in the permittivity field. As mentioned above, Eq. (7) is a formal solution to the Helmholtz equation, as the unknown function U is on both sides of the equation. Practical solutions deal with various approximations made in the integral on right-hand side of Eq. (7). We have already imposed an approximation to make the boundary conditions manageable. The typical approach is to use a perturbation-theoretic method. It is easy to show this if we consider Eq. (7) as an operator equation (Evans et al., 2000). Define the operator g such that

$$g = k^2 \int G\, \varepsilon' \tag{8}$$

So that Eq. (7) becomes

$$U = U_0 + g\, U \tag{9}$$

which can also be written as

$$U = (1 - g)^{-1}\, U_0 = \left(1 + \sum_{n=1}^{\infty} g^n\right) U_0 \tag{10}$$

Note that the convergence of this series requires that $|g| < 1$, and for any useful practical solution, $|g| \ll 1$. (The vertical bars indicate an operator norm.) So, in principle the solution to the Lippmann-Schwinger equation boils down to finding the operator g. Let

$$g^1 \equiv k^2 \int G_0\, \varepsilon' \tag{11}$$

where G_0 is the free-space Green's function, given by the solution to

$$\left(\nabla^2 + k^2\right) G_0 \left(\boldsymbol{r} - \boldsymbol{r}'\right) = -\delta \left(\boldsymbol{r} - \boldsymbol{r}'\right) \tag{12}$$

In three dimensions, it can be shown that

$$G_0 \left(\boldsymbol{r} - \boldsymbol{r}'\right) = \frac{e^{ik\|\boldsymbol{r}-\boldsymbol{r}'\|}}{4\,\pi\, \|\boldsymbol{r} - \boldsymbol{r}'\|} \tag{13}$$

where the double vertical lines refer to the magnitude of the vector. Therefore, g, and hence the solution to the Lippmann-Schwinger equation only requires the specification of the unknown permittivity deviation field. Since

$$g^n = \left(k^2 \int G_0 \, \varepsilon' \right)^n \tag{14}$$

Equation (7) can be written as the series

$$\begin{aligned} U(\mathbf{r}) &= \left[\sum_{n=0}^{\infty} \left(k^2 \int G_0 \, \varepsilon' \right)^n \right] U_0 \\ &= U_0(\mathbf{r}) + k^2 \int G_0(\mathbf{r} - \mathbf{r}') \, \varepsilon'(\mathbf{r}') \, U_0(\mathbf{r}') \, d\mathbf{r}' \\ &+ k^4 \int G_0(\mathbf{r} - \mathbf{r}') \, G_0(\mathbf{r}' - \mathbf{r}'') \, \varepsilon'(\mathbf{r}') \, \varepsilon'(\mathbf{r}'') \, U_0(\mathbf{r}'') \, d\mathbf{r}' \, d\,\mathbf{r}'' \\ &+ \ldots \end{aligned} \tag{15}$$

where the explicit use of position labels is used to show the correct dependency, and we have also defined $g^0 = 1$. This series solution is formally a Neumann series solution to a Fredholm integral equation – here, the Lippmann-Schwinger equation. In scattering theory, the series is known as the Born series and the first two terms constitute the widely-used first-order Born approximation. Given small ε', a perturbation approach can also be used to derive the Born series. Let

$$U = \sum_{n=0}^{\infty} \alpha^n \, U_n \tag{16}$$

where $\alpha < 1$. We also set $\varepsilon' \rightarrow \alpha \varepsilon'$. Plugging these into the Lippmann-Schwinger integral equation gives

$$\sum_{n=0}^{\infty} \alpha^n \, U_n(\mathbf{r}) \approx U_0(\mathbf{r}) + k^2 \int G(\mathbf{r} - \mathbf{r}') \, \alpha \, \varepsilon'(\mathbf{r}') \sum_{n=0}^{\infty} \alpha^n \, U_n(\mathbf{r}') \, d\mathbf{r}' \tag{17}$$

Title Page
Abstract | Introduction
Conclusions | References
Tables | Figures
◄| |►
◄ ►
Back | Close
Full Screen / Esc
Printer-friendly Version
Interactive Discussion

In order to equate equal powers of α, the sum inside the integral must be of the form, $\sum\limits_{n=1}^{\infty} \alpha^{n-1} U_{n-1}(\mathbf{r}')$, which gives

$$\sum_{n=0}^{\infty} \alpha^n \, U_n \, (\mathbf{r}) \approx U_0 \, (\mathbf{r}) + k^2 \int G(\mathbf{r} - \mathbf{r}') \, \alpha \varepsilon'(\mathbf{r}') \sum_{n=1}^{\infty} \alpha^{n-1} \, U_{n-1} \, (\mathbf{r}') \, d\mathbf{r}' \tag{18}$$

or,

$$\begin{aligned} U_1 \, (\mathbf{r}) &\approx U_0 \, (\mathbf{r}) + k^2 \int G_0 \, (\mathbf{r} - \mathbf{r}') \, \varepsilon'(\mathbf{r}') \, U_0 \, (\mathbf{r}') \, d\mathbf{r}' \\ U_2 \, (\mathbf{r}) &\approx U_1 \, (\mathbf{r}) + k^2 \int G_0 \, (\mathbf{r} - \mathbf{r}') \, \varepsilon'(\mathbf{r}') \, U_1 \, (\mathbf{r}') \, d\mathbf{r}' \\ &= U_0 \, (\mathbf{r}) + k^2 \int G_0 \, (\mathbf{r} - \mathbf{r}') \, \varepsilon'(\mathbf{r}') \, U_0 \, (\mathbf{r}') \, d\mathbf{r}' \\ &+ k^2 \int G_0 \, (\mathbf{r} - \mathbf{r}') \left[k^2 \int G_0 \, (\mathbf{r}' - \mathbf{r}'') \, \varepsilon' \, (\mathbf{r}'') \, U_0 \, (\mathbf{r}'') \, d \, \mathbf{r}'' \right] \varepsilon'(\mathbf{r}') \, d\mathbf{r}' + \ldots \end{aligned} \tag{19}$$

So we see that the n-th term in this series is the same as the n-th term in Eq. (15).

2.1 Rytov approximation

The Rytov approximation is an alternative to the Born approximation. In the literature, it is felt that the Rytov method is preferable for long-path forward scattering problems; hence this is the method of choice for the GNSS-LEO occultation problem. We return to the Helmholtz wave equation and let

$$U(\mathbf{r}) = e^{\psi(\mathbf{r})} \tag{20}$$

where the complex phase, ψ, is given by

$$\psi \, (\mathbf{r}) = \chi \, (\mathbf{r}) + i \, S \, (\mathbf{r}) \tag{21}$$

and χ is the so-called log-amplitude function, and S is the phase function. Plugging Eq. (20) into Eq. (1) gives

$$\nabla^2 \, \psi + \nabla \, \psi \cdot \nabla \, \psi + k^2 \, \varepsilon = 0 \tag{22}$$

This is a non-linear equation of the Riccati type. In order to obtain the Rytov approximation, we begin with Eq. (22) and let $\psi = \sum_{n=0}^{\infty} \alpha^n \psi_n$ and $\varepsilon \rightarrow 1 + \alpha\varepsilon'$, as with the Born approximation. Plugging this into Eq. (22) gives

$$\nabla^2 \sum_{n=0}^{\infty} \alpha^n \psi_n + \nabla \sum_{n=0}^{\infty} \alpha^n \psi_n \cdot \nabla \sum_{m=0}^{\infty} \alpha^m \psi_m + k^2 (1 + \alpha \varepsilon') = 0 \tag{23}$$

Consider the first two terms. Equating equal powers of α to zero, gives

$$\begin{aligned} \nabla^2 \psi_0 + \nabla \psi_0 \cdot \nabla \psi_0 + k^2 &= 0 \\ \nabla^2 \psi_1 + 2 \nabla \psi_0 \cdot \nabla \psi_1 + k^2 \varepsilon' &= 0 \end{aligned} \tag{24}$$

As mentioned above, these are nonlinear equations of the Riccati type. However, we can recast them as Helmholtz-type equations by solving for $U_0\psi_n$ instead of ψ_n. Noting that

$$\nabla^2 U_0 \psi_n = U_0 \nabla^2 \psi_n + \psi_n \nabla^2 U_0 + 2 \nabla U_0 \cdot \nabla \psi_n \tag{25}$$

and since $U_0 = e^{\psi_0}$ this means that $\nabla U_0 = U_0 \nabla \psi_n$, this equation becomes

$$\nabla^2 U_0 \psi_n = U_0 \nabla^2 \psi_n + \psi_n \nabla^2 U_0 + 2 U_0 \nabla \psi_0 \cdot \nabla \psi_n \tag{26}$$

Now, let's compute the first-order term. Using Eq. (24), $\nabla^2 \psi_1 = -2\nabla\psi_0 \cdot \nabla\psi_1 - k^2\varepsilon'$, and the first-order Helmholtz equation, $\nabla^2 U_0 = -k^2 U_0$, Eq. (26) becomes

$$\left(\nabla^2 + k^2\right) U_0 \psi_1 = U_0 \left(-k^2 \varepsilon' - 2 \nabla \psi_0 \cdot \nabla \psi_1 + 2 \nabla \psi_0 \cdot \nabla \psi_1\right) = -k^2 \varepsilon' U_0 \tag{27}$$

It can be seen that this is now Helmholtz equations for $U_0\psi_1$. We can now solve these via the integral methods shown above,

$$\psi_1 (\mathbf{r}) = \frac{k^2}{U_0 (\mathbf{r})} \int G_0 (\mathbf{r} - \mathbf{r}') \, \varepsilon'(\mathbf{r}') \, U_0 (\mathbf{r}') \, d\mathbf{r}' \tag{28}$$

This is known as the first Rytov approximation.

2.2 Random media

So far, we have not said much about the permittivity field excepting for its typical scales and magnitudes. We have shown above, that in principle the Helmholtz wave equation, and its various approximations, contains all the information needed to handle deterministic fields: refraction via geometrical optics and scattering via the Born or Rytov approximations. Now we turn to the problem of a random permittivity field using the first Rytov approximation (ψ_1). Clearly, there is an ambiguity in defining the term random in the current context. Over long enough time scales and over a wide range of spatial scales, one can consider the atmosphere to be random – it is just the nature of the Navier-Stokes equations. For the problem at hand, we are considering relatively short time scales; hence to "see" the randomness, the spatial scales must also be relatively small (think of eddy turnover time). Hence, the permittivity scales that produce refraction in the waves will be considered to be deterministic. Typically, smaller scales will be random, except for some layered media which may have large longitudinal scales, but small vertical ones. In the middle will be scales that will be ambiguous as to whether they are due to a deterministic phenomena or a random one. This may be important in practical applications, specifically in using models of the atmospheric structure. For now, we will be content to discuss purely random fluctuations.

As mentioned above, we will use the first Rytov approximation as our tool. In this fashion, we will be restricted to small perturbations, which is a reasonable assumption for microwave propagation. For now, we will assume straight-line propagation. Dealing with non-straight line propagation – due to refraction – is beyond the scope of this work. Return to Eq. (28). If it assumed that the scattering angles are small – a reasonable assumption if the ratio λ / l_0 (l_0 is the smallest scale of the permittivity fluctuations.) – we can make the so-called parabolic approximation in the integral equation. Consider a point source (i.e., spherical wave). The factors in the integrand are then

$$G_0\left(\mathbf{r}-\mathbf{r}'\right)\frac{U_0\left(\mathbf{r}'\right)}{U_0\left(\mathbf{r}\right)}=\frac{e^{ik\left\|\mathbf{r}-\mathbf{r}'\right\|}}{4\pi\left\|\mathbf{r}-\mathbf{r}'\right\|}\frac{e^{ik\left(\left\|\mathbf{r}'\right\|-\left\|\mathbf{r}\right\|\right)}\left\|\mathbf{r}\right\|}{\left\|\mathbf{r}'\right\|} \quad (29)$$

Consider the quantity, $\|\boldsymbol{r}-\boldsymbol{r}'\| = \left[(x-x')^2+(y-y')^2+(z-z')^2\right]^{1/2}$. Assuming that the propagation is in the x direction, and that $x-x'$,(the distance along the x-axis from the scatterer to the receiver), is much greater than the transverse distances (valid for small-angle scattering), then this expression can be approximated by

$$\begin{aligned} \|\boldsymbol{r}-\boldsymbol{r}'\| &= (x-x')\left[1+\frac{(y-y')^2+(z-z')^2}{(x-x')^2}\right]^{1/2} \\ &\approx (x-x')+\frac{(y-y')^2+(z-z')^2}{2\,(x-x')} \end{aligned} \tag{30}$$

Similar expansions can be made for the terms $\|\boldsymbol{r}\|$ and $\|\boldsymbol{r}'\|$. Since $k\|\boldsymbol{r}-\boldsymbol{r}'\| = 2\pi\|\boldsymbol{r}-\boldsymbol{r}'\|/\lambda \gg 1$, we will use the full expression in Eq. (30); whereas, we only need to keep the leading term for the non-exponential terms. Plugging all these factors back into Eq. (29), and doing some algebra, gives

$$G_0(\boldsymbol{r}-\boldsymbol{r}')\,\frac{U_0(\boldsymbol{r}')}{U_0(\boldsymbol{r})} \approx \frac{b(x,x')}{4\pi}\exp\left[\frac{i\,k\,b(x,x')}{2}\left\|\frac{x'}{x}\boldsymbol{\rho}-\boldsymbol{\rho}'\right\|^2\right] \tag{31}$$

where, $b(x,x') = \frac{x}{x'(x-x')}$ and $\boldsymbol{\rho} = (y,\ z)$. Inserting this expression into our integral formula gives

$$\psi_1(\boldsymbol{r}) \approx \frac{k^2}{4\pi}\int b(x,x')\exp\left[\frac{i\,k\,b(x,x')}{2}\left\|\frac{x'}{x}\boldsymbol{\rho}-\boldsymbol{\rho}'\right\|^2\right]\varepsilon'(\boldsymbol{r}')\,d\boldsymbol{r}' \tag{32}$$

Next, consider the transmitter, receiver and atmosphere all moving relative to each other – and all with respect to a fixed coordinate system, e.g., the center of the Earth. Note that we are assuming that the "x"-positions are not changing. This is due to the fact that these motions do not change the value of the complex phase, $\psi_1(\boldsymbol{r})$, in an appreciable manner. We consider a short enough time interval, τ, such that $\boldsymbol{\rho}\,(t_2) = \boldsymbol{\rho}\,(t_1) + \boldsymbol{V}\tau$. Where $\boldsymbol{V}$ is the projection of the velocity vector of the receiver into the plane perpendicular to x. Actually, if we define $\boldsymbol{V}$ as the average velocity over τ, then this expression holds for any time interval. Now for some notation. $\boldsymbol{r} = (x,\ \boldsymbol{\rho})$ is the location of the receiver at any given time, so we will use the notation $\boldsymbol{\rho} = \boldsymbol{\rho}_R$ and $\boldsymbol{V}_{\mathrm{R}}$ for the velocity vector of the receiver. Similarly, $\boldsymbol{r}' = (x',\ \boldsymbol{\rho}')$ is the position of a scatterer, with average velocity $\boldsymbol{V}_{\mathrm{S}}$. Finally, $\boldsymbol{\rho}_{\mathrm{T}}$ and $\boldsymbol{V}_{\mathrm{T}}$ are the transverse position and velocity of the transmitter. Hence, we can write Eq. (32) at two times, t_1 and t_2 ($\tau = t_2 - t_1$), as

$$\psi_1\,(x,\ \boldsymbol{\rho}_{\mathrm{R}}(t_1)) \approx \frac{k^2}{4\,\pi} \int b\left(x,\ x'\right)\ \exp\left[\frac{i\ k\ b\left(x,\ x'\right)}{2}\right. \\ \left.\left\|\frac{x'}{x}\ \boldsymbol{\rho}_{\mathrm{R}}(t_1) - \boldsymbol{\rho}'(t_1) + \left(1 - \frac{x'}{x}\right)\ \boldsymbol{\rho}_{\mathrm{T}}(t_1)\right\|^2\right]\ \varepsilon'\left(\boldsymbol{r}'(t_1)\right)\ d\boldsymbol{r}' \tag{33}$$

and

$$\psi_1\,(x,\ \boldsymbol{\rho}_{\mathrm{R}}(t_2)) \approx \frac{k^2}{4\,\pi} \int b\left(x,\ x''\right)\ \exp\left[\frac{i\ k\ b\left(x,\ x''\right)}{2}\right. \\ \left.\left\|\frac{x''}{x}\left(\boldsymbol{\rho}_{\mathrm{R}}\,(t_1) + (\boldsymbol{V}_{\mathrm{R}} - \boldsymbol{V}_{\mathrm{T}})\,\tau\right) - (\boldsymbol{V}_{\mathrm{S}} - \boldsymbol{V}_{\mathrm{T}})\,\tau - \boldsymbol{\rho}''\,(t_1) + \left(1 - \frac{x''}{x}\right)\boldsymbol{\rho}_{\mathrm{T}}(t_1)\right\|^2\right]\ \varepsilon'(\boldsymbol{r}''(t_2))\ d\boldsymbol{r}'' \tag{34}$$

Except for ε', both equations are now expressed in terms of t_1, so we can drop that notation except for where it is needed explicitly. The important distinction between deterministic and random quantities is that the latter should only be quantified via its statistical properties. For our purposes, we will consider second-order correlation functions – and later with their associated Fourier frequency spectrum.

Recalling that $\psi_1 = \chi_1 + iS_1$, let us compute the correlation function of the log-amplitude field,

$$B_{\chi_1}\,(\boldsymbol{\rho}_{\mathrm{R}}(t_1),\ \boldsymbol{\rho}_{\mathrm{R}}(t_2)) = \frac{1}{2}\left[Re\ \langle\psi_1(\boldsymbol{\rho}_{\mathrm{R}}(t_1))\ \psi_1(\boldsymbol{\rho}_{\mathrm{R}}(t_2))\rangle \right. \\ \left. + Re\ \left\langle\psi_1(\boldsymbol{\rho}_{\mathrm{R}}(t_1))\ \psi_1^*(\boldsymbol{\rho}_{\mathrm{R}}(t_2))\right\rangle\right] \tag{35}$$

where the angled brackets refer to a probability (ensemble) average. Next, we apply Taylor's Hypothesis to the field $\varepsilon'(\boldsymbol{r}''(t_2)) = \varepsilon'(\boldsymbol{r}''(t_1) + \boldsymbol{V}_{\mathrm{s}}\tau)$. This hypothesis assumes that due to pure advection, $\varepsilon'(\boldsymbol{r}''(t_2)) = \varepsilon'(\boldsymbol{r}''(t_1))$. That is, the permittivity fluctuation due to a scatterer at $\boldsymbol{r}''(t_1)$ will have the same numerical value after it drifts to $\boldsymbol{r}''(t_2)$. This is the reason Taylor's Hypothesis is often referred to as the "frozen-in" property. Next, we impose the so-called Markov approximation. Consider the correlation function of the permittivity field

$$B_{\varepsilon'}(x', x'', \boldsymbol{\rho}', \boldsymbol{\rho}'') = \langle \varepsilon'(x', \boldsymbol{\rho}')\, \varepsilon'(x'', \boldsymbol{\rho}'') \rangle \tag{36}$$

For a homogeneous field, this can only be a function of $\boldsymbol{\rho}' - \boldsymbol{\rho}''$ and $x' - x''$, and furthermore if the field is also isotropic it can only be a function of $\|\boldsymbol{\rho}' - \boldsymbol{\rho}''\|$ and $|x' - x''|$. The Markov approximation states there is no correlation of the permittivity field in the longitudinal direction (i.e., it is a Markov process), and hence

$$B_{\varepsilon'}(x', x'', \boldsymbol{\rho}', \boldsymbol{\rho}'') = \delta(|x' - x''|)\, A_{\varepsilon'}(\|\boldsymbol{\rho}' - \boldsymbol{\rho}''\|) \tag{37}$$

where $A_{\varepsilon'}$ is the correlation function in the transverse coordinates. Next, Eqs. (33), (34) and (37) are inserted into Eq. (35). In order to compute the integrals, we make the following changes in variables: $\xi = x' - x''$, $\eta = \left(x' + x''\right)/2$ and then integrate over ξ; $\boldsymbol{\alpha} = \boldsymbol{\rho}' - \boldsymbol{\rho}''$, $\boldsymbol{\beta} = \left(\boldsymbol{\rho}' + \boldsymbol{\rho}''\right)/2$ and integrate over $\boldsymbol{\beta}$. Let $\boldsymbol{V}_{\mu} = \left(\eta/R\right)(\boldsymbol{V}_{\mathrm{R}} - \boldsymbol{V}_{\mathrm{T}}) - (\boldsymbol{V}_{\mathrm{S}} - \boldsymbol{V}_{\mathrm{T}})$, where R is the distance between the transmitter and receiver along the x-axis. Finally, use the expression

$$A_{\varepsilon'}\left(\|\boldsymbol{\alpha}\|\right) = 2\pi \int e^{i\boldsymbol{q}\cdot\boldsymbol{\alpha}}\, \varphi_{\varepsilon'}\left(0, \|\boldsymbol{q}\|\right) d\boldsymbol{q} \tag{38}$$

where, $\varphi_{\varepsilon'}(q_x, \|\boldsymbol{q}\|)$ is the three-dimensional spatial spectrum of the isotropic permittivity fluctuations and $\boldsymbol{q} = \left(q_y, q_z\right)$. Plugging all of these quantities into Eq. (35) and performing various intermediary integrations, gives the desired result

$$B_{\chi_1}\left(\boldsymbol{\rho}_{\mathrm{R}}(t_1), \boldsymbol{\rho}_{\mathrm{R}}(t_2)\right) = 4\,\pi^2\,k^2 \int \varphi_{\varepsilon'}(0, \|\boldsymbol{q}\|)\, J_0(\|\boldsymbol{q}\|\|\boldsymbol{V}_\mu\|\,\tau) \sin^2\left(\frac{\|\boldsymbol{q}\|^2}{2k\; b(\eta)}\right)\|\boldsymbol{q}\|d\|\boldsymbol{q}\|d\eta \tag{39}$$

The correlation function of the phase fluctuations follows the same procedure, excepting Eq. (35) is replaced by

$$B_{S_1}(\boldsymbol{\rho}_{\mathrm{R}}(t_1), \boldsymbol{\rho}_{\mathrm{R}}(t_2)) = \frac{1}{2}\left[Re\left\langle \psi_1(\boldsymbol{\rho}_{\mathrm{R}}(t_1))\; \psi_1^*(\boldsymbol{\rho}_{\mathrm{R}}(t_2))\right\rangle - Re\,\langle \psi_1(\boldsymbol{\rho}_{\mathrm{R}}(t_1))\; \psi_1(\boldsymbol{\rho}_{\mathrm{R}}(t_2))\rangle\right] \tag{40}$$

which leads to an equation similar to Eq. (39), excepting that the sine-squared term is replaced by a cosine-squared one.

To compute the frequency spectrum, we take the cosine transform of Eq. (39). We define the cosine transform of a function $g(t)$ as

$$g(f) = 4\int_0^\infty g(t)\cos(2\pi\, f t)\, dt \tag{41}$$

Instead of using the spectrum of the permittivity field we shall henceforth use the more commonly used spectrum of the index of refraction field, $\varphi_{n'}$. For weak scattering, $\varphi_{\varepsilon'} \approx 4\varphi_{n'}$. Hence,

$$\varphi_{\chi_1}(f) = 16\,\pi^2\,k^2 \int \varphi_{n'}(0, \|\boldsymbol{q}\|)\, J_0(\|\boldsymbol{q}\|\|\boldsymbol{V}_\mu\|\,\tau)\, \sin^2\left(\frac{\|\boldsymbol{q}\|^2}{2k\; b(\eta)}\right) \cos(2\,\pi\, f\, \tau)\, \|\boldsymbol{q}\|\, d\|\boldsymbol{q}\|\, d\eta\, d\tau \tag{42}$$

After performing the integration over $\|\boldsymbol{q}\|$ we get (Cornman et al., 2009)

$$\varphi_{\chi_1}(f) = \int\limits_{\eta_1-\Delta\eta/2}^{\eta_1+\Delta\eta/2} \frac{16\,\pi^{5/2}\,k^2\,A\,C_{n'}^2(\eta)}{V_\mu(\eta)}\,\tilde{y}^{-4/3}\left\{\frac{2\,\Gamma(1/3)}{5\,\Gamma(5/6)} - Re\left[e^{ia\tilde{x}^2}U\left[1/2,-1/3,-ia\tilde{y}\right]\right]\right\}d\eta \tag{43}$$

where we have used the isotropic von Karman form for the index of refraction spectrum

$$\varphi_{n'}\left(0,\,\|\boldsymbol{q}\|^2\right) = A\,C_{n'}^2(\eta)\left[\|\boldsymbol{q}\|^2 + \left(2\,\pi/L\right)^2\right]^{-11/6} \tag{44}$$

where A is a constant, $C_{n'}^2(\eta)$ is the intensity of the turbulence ("structure constant") at the point η, R is the distance along the line of sight from the transmitter to the receiver, k is the transmitter wavenumber, and L is a length scale related to the correlation function for the index of refraction field. Also in Eq. (43), we are assuming a patch of turbulence centered at $\eta=\eta_1$ with extent $\Delta\eta$; and we have denoted $a=\eta(R-\eta)/kR$, $\tilde{x}=2\pi f/V_\mu$, $\tilde{y}=\tilde{x}^2+L^{-2}$; Γ is the gamma function, and U is the confluent hypergeometric function of the second kind. The frequency spectrum of the phase is given by an expression similar to Eq. (42), excepting that the minus sign in the curly brackets is replaced by a plus sign. If the turbulence patch is narrow enough along the line of sight, then the integral over η can be approximated by a simple mid-point formula,

$$\varphi_{\chi_1}(f) \approx \frac{16\,\pi^{5/2}\,k^2\,A\,C_{n'}^2(\eta_1)\,\Delta\eta}{V_\mu(\eta_1)}\,\tilde{y}^{-4/3}\left\{\frac{2\,\Gamma(1/3)}{5\,\Gamma(5/6)} - Re\left[e^{ia\tilde{x}^2}\,U\left[1/2,\,-1/3,\,-ia\,\tilde{y}\right]\right]\right\} \tag{45}$$

where $a=a\,(\eta_1)$, $\tilde{x}=\tilde{x}\,(\eta_1,\,f)$ and $\tilde{y}=\tilde{y}\,(\eta_1,\,f,\,L)$. A discussion of the appropriateness of this approximation is beyond the scope of this paper.

Figures 1, 2, and 3 illustrate the sensitivity of Eq. (45) to variations in $C^2_{n'}(\eta_1)\Delta\eta$ (denoted, $C^2_{n'}$ for simplicity), η_1, and L, respectively. Since it is a multiplicative factor, $C^2_{n'}(\eta_1)\Delta\eta$ simply changes the overall amplitude of the spectrum. The changes in η_1 are more complicated, effecting both the amplitude and the locations in frequency of the oscillations – as can be seen more pronouncedly in Fig. 2 between 1 and 2 Hz. Figure 3 illustrates the effect due to changes in the turbulence length scale, essentially raising or lowering the spectral amplitudes at the lowest frequencies. As can be seen from these figures, the variations in these parameters are not distinct, i.e., changes in one parameter can look like changes in another one. This fact makes parameter estimation difficult, as will be discussed subsequently.

For isotropic fluctuations in the permittivity field, all the results presented above are applicable to the non-neutral atmosphere – excepting for changes in the constants. Most importantly, due to dispersion effects in a conducting field the functionality on the transmitter wavenumber for the frequency spectrum, is to first order k^{-2}, as opposed to k^2 in the neutral atmosphere. Furthermore, in the ionosphere, alignment along the direction of the geomagnetic field can produce anisotropic fluctuations in the electron density field – and hence the permittivity field. To accommodate this fact, anisotropic models of the permittivity field can be used (Yeh and Liu, 1982; Tereshchenko et al., 2004). These models, however, assume the same anisotropic form for all wavenumbers. This is a questionable assumption, as the tendency towards isotropy at small spatial scales is more expected. Another approach is to use an anisotropic model, which has different outer length scales along each coordinate axis (Kristensen et al., 1989). This model will then approach isotropy for large wavenumbers. The integrals over wavenumber in the equations presented above also need to be modified, i.e., the single integral over $q = \|\boldsymbol{q}_\perp\|$ is replaced with a double integral over $q_{y\perp}$ and $q_{z\perp}$, where these are orthogonal components of the wavevector in the plane perpendicular to the propagation direction. Gravity waves driven by topography or convective processes can propagate upwards (and intensify) from the troposphere into the stratosphere; hence, some authors have adopted a hybrid model for the index of refraction power spectrum. This model is the sum of an isotropic spectrum (e.g., Eq. 44 above) and an anisotropic model representing a random superposition of internal gravity waves (Gurvich and Chunchuzov, 2003).

3 Parameter estimation

Assuming that the received signal is a Gaussian random process, its spectral values at each frequency will have an exponential distribution. It is important to note that this randomness is due to the random permittivity field – not the additive receiver and processing noise. Using the fact that the spectral points are exponentially distributed, numerous realizations of the spectra can be generated, i.e., by replacing each spectral point with a sample from an exponentially distributed random number sequence. An example of this is shown in Fig. 4. The exponential probability density function is given by,

$$P(x) = \frac{1}{\beta} e^{-x/\beta} \tag{46}$$

where β is the mean value for the distribution. For an exponential distribution, the standard deviation is equal to the mean. Hence, for the simulation, the spectral level at a given frequency is given by replacing that point by a sample from an exponential distribution with its mean value being the theoretical spectral value at that point (i.e., from Eq. 44). The probability distribution function is given by,

$$P(x \le b) = \int_0^b P(x)\, dx = \frac{1}{\beta} \int_0^b e^{-x/\beta}\, dx = 1 - e^{-b/\beta} \tag{47}$$

If $b = \beta$, $P(x \le \beta) = 1 - e^{-1} \approx 0.63$; hence, more often than not, samples from a exponential distribution will be less than its mean, as can be seen in Fig. 4. The simulation is intended to represent real-world situations; hence, it was assumed that the received signal would be available at 50 Hz, and approximately 10 s worth of data would go into a single spectrum. The parameters used in the simulation are: $C_{n'}^2 \Delta\eta = 4 \times 10^{-9}$, $L = 5$ km, and $\eta_1 = 20\,200$ km. Furthermore, a noise floor, $Q = 3.5 \times 10^{-5}$, is added to the data. The magnitude of this level is derived from COSMIC GNSS-LEO data.

Referring back to Eq. (45), the parameters to be estimated are $C_{n'}^2(\eta_1)\Delta\eta$, L, η_1 and Q: the turbulence intensity, the turbulence length scale, the location of the center of the turbulence patch from the transmitter, and the noise level. As the functional form of Eq. (45) is highly non-linear in L and η_1, a simultaneous solution for all four parameters is complicated. The preferred solution is via the maximum likelihood (ML) method. It is known that the ML method is asymptotically unbiased and has minimum variance, asymptotically (Freund, 1992). Consider a model of the form,

$$\mu_i = c\,\varphi_i(\eta_1, L) + Q \tag{48}$$

where "i" refers to the frequency, f_i, $c = C_{n'}^2(\eta_1)\Delta\eta$, and φ_i is the right-hand side of Eq. (45), divided by c. Consider a measured spectrum, denoted X_i. It is assumed that the X_i are independent exponential random variables with expected values, $\langle X_i \rangle = \mu_i$. The likelihood function is then given by

$$L = \frac{e^{-\sum\limits_{i=1}^{N} \frac{X_i}{\mu_i}}}{\prod\limits_{i=1}^{N} \mu_i} \tag{49}$$

where, N is the number of frequency values. The negative log-likelihood function is

$$-\ln L = \sum_{i=1}^{N} \left[\frac{X_i}{\mu_i} + \ln \mu_i \right] \tag{50}$$

The ML estimates for the parameters are found by solving the coupled set of non-linear equations, $\partial(-\ln L)/\partial p_j = 0$, where the p_j are the parameters, c, Q, L and

η_1, respectively. Instead of dealing with this formidable problem, a simpler two-dimensional problem will be discussed to motivate the techniques. It will be assumed that L is known. Since the model, μ_i, is linear in c and Q, a linear weighted least squares approach can be employed to estimate those two parameters. Once that is done, these values can then be used in a one-dimensional ML solution for η_1. Some variations on this approach can also be used, and will be discussed below. Consider the least squares problem for c and Q. It will be the simultaneous solution to the coupled equations, $\partial R/\partial p_j = 0$, $(p_j = \{c, Q\})$, where $R = \sum_{i=1}^{N} (\mu_i - X_i)^2 w_i$, and the weights w_i are independent of c and Q. If the weights are chosen such that $w_i = \varphi_i^{-1}$, then this is similar to a chi-squared minimization problem. The solution for the parameters can then be solved via Cramer's method for a 2x2 system of equations, giving

$$c = \frac{\sum\limits_{i,j=1}^{N} \frac{X_i}{\varphi_j} - N \sum\limits_{i=1}^{N} \frac{X_i}{\varphi_i}}{\sum\limits_{i,j=1}^{N} \frac{\varphi_i}{\varphi_j} - N^2}, \quad Q = \frac{\sum\limits_{i,j=1}^{N} \frac{\varphi_i X_j}{\varphi_j} - N \sum\limits_{i=1}^{N} X_i}{\sum\limits_{i,j=1}^{N} \frac{\varphi_i}{\varphi_j} - N^2} \tag{51}$$

An alternate is to calculate Q directly from the high-frequency parts of X_i. Denoting this estimate, $\bar{Q}$, a 1-D weighted least squares methods gives

$$c = \frac{\sum\limits_{i=1}^{N} (X_i - \bar{Q})}{\sum\limits_{i=1}^{N} \varphi_i} \tag{52}$$

A further alternative – the one that will be employed in the following – is to calculate c via a "pseudo" ML method. That is, we assume that the data X_i is replace by $\bar{X}_i = X_i - \bar{Q}$, and then solve for c via the ML formula, $\partial(-\ln L)/c = 0$. Letting $\bar{\mu}_i = c\varphi_i$

$$\frac{\partial}{\partial c}\sum_{i=1}^{N}\left[\frac{\bar{X}_i}{\bar{\mu}_i}+\ln\bar{\mu}_i\right]=-\sum_{i=1}^{N}\left[\frac{\bar{X}_i}{\varphi_i}\right]+N\,c \tag{53}$$

Equating this to zero, gives the desired ML-like estimate for c,

$$c\,(\eta)=\frac{1}{N}\sum_{i=1}^{N}\frac{\bar{X}_i}{\varphi_i(\eta)}=\frac{1}{N}\sum_{i=1}^{N}\frac{X_i-\bar{Q}}{\varphi_i(\eta)} \tag{54}$$

Plugging this back into Eq. (49) gives

$$-\ln L\,(\eta)\;=\;N\,[1+c\,(\eta)]+\sum_{i=1}^{N}\ln\varphi_i\,(\eta) \tag{55}$$

or, explicitly

$$-\ln L\,(\eta)\;=\;N+\sum_{i=1}^{N}\frac{\bar{X}_i}{\varphi_i\,(\eta)}+\sum_{i=1}^{N}\ln\varphi_i\,(\eta) \tag{56}$$

where the explicit dependence on η has been indicated. (Recall that we are not including dependence on L at this point). Note that the last term is independent of the data and can thereby be computed a priori. Equation (55) is now a one-dimensional function and the solution for η_1 is given by minimizing it with respect to η. An analytical form for $\partial(-\ln L)/\partial\eta$ has been calculated, but it is extremely complicated (containing logarithmic derivatives of the hypergeometric function in Eq. (45), and furthermore the noise in the $\bar{X}_i$ is a significant problem. For the results presented below, we merely take the minimum value of Eq. (55) as a function of η as the estimate for η_1. Once the estimate for η_1 is determined, this value is plugged back into Eq. (54) to estimate c. Figure 5 through Fig. 7 show the results of Eq. (56) when varying c, η_1, and L, respectively – as was done in Fig. 2 through Fig. 4. It can be seen that different values of c will shift the negative log-likelihood curves up or down. (For simplicity in terminology, the phrase "likelihood" will mean "negative log-likelihood.") Changes in η_1 and L

change the likelihood function in more complicated fashions, not only varying the level of the curves, but also their shape. Figure 8 illustrates Eq. (54) for the case where the theoretical spectrum, Eq. (45), plus the noise floor is used for X_i. As will be shown below, this is the expected value for the estimator. It can be seen that this function varies an order of magnitude over the chosen range of η values (15 000–25 000 km). Figure 9 shows the first term in the likelihood function, Eq. (55) and Fig. 10 shows the second term. Obviously, the sum of these two functions gives the likelihood function – as seen in the black curve in Fig. 5. The asymmetry in the likelihood function is due to the fact that the slopes of the two curves (first and second terms) are similar in magnitude, but opposite in sign for smaller η values; whereas the slope of the first term is decreasing more rapidly than that of the second term at larger η values. Therefore, the sum of the two terms is almost flat for smaller η values and rises more rapidly at larger ones. The flatness of the likelihood function at the smaller η poses a problem for the η_1 estimation – one would like a steep bowl leading down to the correct minimum. The flatness means that wiggles in the likelihood function – due to the exponentially distributed random errors in the spectral values – can cause a false minimum to be smaller than one for the true minimum. A simple method was developed to deal with this problem: using a weighting function in the denominator of Eq. (54). This function is solely dependent on η. The only portions of the line of sight that are of interest are those that go through the atmosphere or at least portions of it where turbulence can be strong enough to disturb the signal significantly. For example, excluding outer regions of the ionosphere where the permittivity perturbations due to fluctuations in the electron density field are small. Hence, the weighting function can be chosen such that it is close to one for those portions of interest along the line of sight, and drops smoothly to zero away from those regions. An example of such a weighting function is shown in Fig. 11, and its effect on the likelihood function is illustrated in Fig. 12. It can be seen that the likelihood function is unchanged essentially, between approximately 18 000 to 22 000 km. This is important, as the purpose here is not to bias the estimates, but to try to eliminate outliers.

In order to examine the statistical properties of the c and η_1 estimators, 1000 realizations of the simulated spectra – as was seen in Fig. 1 – were generated. Before discussing these results, however, some preliminary concepts are presented.

3.1 Theoretical error analysis

Since the random errors in η_1 are not easily described theoretically, these will be analyzed in the context of the simulation results. Consider then the estimator for c, as given by Eq. (54). Recall that this was referred to as a pseudo-ML estimator. This is because the correct ML estimate is given by using

$$-\ln L = \sum_{i=1}^{N} \left[\frac{X_i}{c\,\varphi_i + Q} + \ln\left(c\,\varphi_i + Q\right) \right] \tag{57}$$

Then, c is found by solving

$$0 = \frac{\partial(-\ln L)}{\partial c} = \sum_{i=1}^{N} \left[-\frac{X_i}{\left(c\,\varphi_i + Q\right)^2\,\varphi_i} + \frac{\varphi_i}{c\,\varphi_i + Q} \right] \tag{58}$$

which is now non-linear in c, thus requiring a numerical solution. The statistical properties of the estimator given by Eq. (54) can be studied. First, consider the expected value of c,

$$\langle c \rangle = \frac{1}{N} \sum_{i=1}^{N} \frac{\langle X_i \rangle - \langle \bar{Q} \rangle}{\varphi_i\,(\eta_1)} = \frac{1}{N} \sum_{i=1}^{N} \frac{\mu_i - Q}{\varphi_i\,(\eta_1)} = \frac{1}{N} \sum_{i=1}^{N} \frac{c\,\varphi_i\,(\eta_1) + Q - Q}{\varphi_i\,(\eta_1)} = c \tag{59}$$

Showing that this is an unbiased estimator of c (where it has been assumed that $\bar{Q}$ is an unbiased estimator of Q, and η_1 is the true value for that parameter). Next, consider the variance of c – with the same assumptions made above

$$\mathrm{Var}\,(c) = \mathrm{Var}\left(\sum_{i=1}^{N} \frac{\bar{X}_i}{N\,\varphi_i\,(\eta_1)} \right) \tag{60}$$

Title Page
Abstract Introduction
Conclusions References
Tables Figures
◀| |▶
◀ ▶
Back Close
Full Screen / Esc
Printer-friendly Version
Interactive Discussion

It can be shown that the variance for a linear combination of independent random variables, γ_i, is given by (Freund, 1992; p. 175),

$$\mathrm{Var}\left(\sum_i a_i\,\gamma_i\right) = \sum_i a_i^2\,\mathrm{Var}\,(\gamma_i) \tag{61}$$

Hence, with $a_i = 1/(N\varphi_i)$, Eq. (60) becomes

$$\mathrm{Var}\,(c) = \frac{1}{N^2}\sum_{i=1}^{N}\frac{\mathrm{Var}\,(\bar{X}_i)}{[\varphi_i\,(\eta_1)]^2} \tag{62}$$

Since it has been assumed that the X_i are independent, exponentially distributed random variables, their variance is equal to the square of their mean, and Eq. (62) becomes

$$\mathrm{Var}\,(c) = \sum_{i=1}^{N}\frac{\left(c\,\varphi_i\,(\eta_1)\,+\,\bar{Q}\right)^2}{N^2\,\varphi_i^2\,(\eta_1)} \tag{63}$$

Note that if $\bar{Q} = 0$, $\mathrm{Var}(c) = c^2/N$.

Things are more complicated when η_1 is not the true value of that parameter. Denote this, $\bar{\eta}_1$. The estimated value for c (denoted $\bar{c}$) is now

$$\langle\bar{c}\rangle = \frac{c}{N}\sum_{i=1}^{N}\frac{\varphi_i\,(\eta_1)}{\varphi_i\,(\bar{\eta}_1)} \tag{64}$$

and hence the bias, $b = \langle c\rangle - \langle\bar{c}\rangle$ is given by

$$b = c\left[1 - \frac{1}{N}\sum_{i=1}^{N}\frac{\varphi_i\,(\eta_1)}{\varphi_i\,(\bar{\eta}_1)}\right] \tag{65}$$

So, it can be seen that the bias is a function of the sum of the ratios of the spectrum evaluated at the true and estimated η_1 values, respectively. Note that if $\bar{\eta}_1 = \eta_1$, then the bias will be zero, as expected.

The variance of $\bar{c}$ is given by Eq. (63), but with $\bar{\eta}_1$ in the denominator. Note that if $Q = 0$, the variance of $\bar{c}$ is

$$\mathrm{Var}\,(\bar{c}) = \left(\frac{c}{N}\right)^2 \sum_{i=1}^{N} \left[\frac{\varphi_i\,(\eta_1)}{\varphi_i\,(\bar{\eta}_1)}\right]^2 \tag{66}$$

Since the X_i are exponentially distributed random variables, the random error is significant – as can be seen in Fig. 4. In order to reduce the random error, averaging spectra is helpful. Consider the statistics of the estimator of c with averaged spectra (denoted $\hat{c}$). The averaged spectral values are given by

$$\hat{X}_i = \frac{1}{M} \sum_{j=1}^{M} (X_i)_j \tag{67}$$

where j indexes the averaging elements – of which there are M. The estimator, $\hat{c}$, is then given by

$$\hat{c} = \frac{1}{N} \sum_{i=1}^{N} \frac{\hat{X}_i}{\varphi_i} = \frac{1}{NM} \sum_{i=1}^{N} \sum_{j=1}^{M} \frac{(X_i)_j}{\varphi_i} \tag{68}$$

Interchanging the order of summation and summing over i gives, $\hat{c} = \sum\limits_{j=1}^{M} c_j/M$. Taking the expected value gives

$$\langle \hat{c} \rangle = \frac{1}{M} \sum_{j=1}^{M} \langle c_j \rangle = \langle c \rangle \tag{69}$$

where it was assumed that the $\langle c_j \rangle$ are identical. This shows that the estimator from the averaged spectra is unbiased. Using Eq. (61), the variance of $\hat{c}$ is given by

$$\mathrm{Var}(\hat{c}) = \mathrm{Var}\left(\sum_{j=1}^{M} c_j/M\right) = \sum_{j=1}^{M} \frac{\mathrm{Var}(c_j)}{M^2} = \frac{\mathrm{Var}(c)}{M} \tag{70}$$

where it was assumed that the variances of c_j are identical. This shows that averaging the spectra reduces the variance of c by a factor of $1/M$.

As seen in Eqs. (64) and (66), the ratio $\varphi_i\,(\eta_1)/\varphi_i\,(\bar{\eta}_1)$ is important in determining the error properties of the estimator $\bar{c}$. In order to study this further, we will need the following concepts. The probability density function for a gamma distribution is given by

$$P(x) = \frac{x^{\alpha-1}\, e^{-x/\beta}}{\beta^{\alpha}\,\Gamma\,(\alpha)} \tag{71}$$

Note that if $\alpha = 1$, we recover the exponential density function, Eq. (46). If X_j is a collection of independent gamma-distributed random variables, with parameters α_i and β, then $\sum_{j=1}^{M} X_j$ are gamma-distributed with parameters $\sum_{j=1}^{M} \alpha_j$ and β. The proof can be found by using the moment generating function for the gamma distribution, $M_X(t) = (1-\beta t)^{-\alpha}$. Since the X_i are independent,

$$M_{\sum X_j} = \prod_{j=1}^{M} (1 - \beta\, t)^{\sum \alpha_j} \tag{72}$$

Since a random variable is uniquely determined by its moment generating function, $\sum_{j=1}^{M} X_j$ is gamma-distributed with parameters $\alpha = \sum_{j=1}^{M} \alpha_j$ and β. Furthermore, if X is gamma-distributed and ν is a positive constant, then νX is gamma-distributed with parameters α and $v\beta$. These properties can now be applied to the problem at hand. Since the spectral values X_i are assumed to be independent, exponentially distributed random variables – or gamma-distributed with $\alpha = 1$ and $\beta = \mu_i$ – it follows that the ratio X_i/μ_i will be exponentially distributed with mean one. (Use the property just discussed, with $v = \mu_i$.) If the μ_i are evaluated with the estimates for Q, c and η_1, then the ratio should be approximately distributed as an exponential distribution with mean one. The same holds for averaging the spectra, but here the ratio $\hat{X}_i/\mu_i$ will be gamma-distributed with $\alpha = M$ and $\beta = 1/M$. (Recall that $\hat{X}_i$ is given by Eq. 67). These properties can then be used to test quality of the estimation methods.

4 Simulation studies

As mentioned above, 1000 independent realizations of the amplitude spectrum were generated. Equation (56) was used to calculate estimates of η_1, and then those are in turn are used to estimate c via Eq. (54), with $\eta = \eta_1$. Recall that the true values for these parameters are $\eta_1 = 20\,200$ and $c = 4 \times 10^{-9}$. There are four different estimation methodologies that were employed, a basic one (as just discussed), one in which a weighting function is used, and then a comparable pair applied to averaged spectra. In the results presented below, five spectra were averaged. A discussion of the overall estimator performance is presented first, followed by a set of case study analyzes that deal with more specific aspects.

4.1 Overall statistical performance

Figures 13 and 14 illustrate the overall simulation results. These are hybrid plots, with both the coloring and widths being related to the number of samples at that specific parameter value (as in a histogram). Furthermore, the smaller purple boxes indicate outliers. Tables 1 and 2 present some descriptive statistics for the results. Most of the statistics used in the tables are order statistics, i.e., quantiles and inter-quantile ranges. These metrics are more robust in the presence of outliers, and so they are more appropriate in this case than metrics such as skewness and kurtosis. It can be seen that the median values are all quite close to the expected value, reflecting the comments above about how the estimators are unbiased. Those comments referred to the estimator for c, but that fact is also represented in the median value of the estimator for η_1. The use of the weighting function has the desired effect: it does not bias the estimates, but it eliminates the most egregious outliers. The effect of spectral averaging on the standard deviation (STD in the tables), is actually greater than that predicted by (the square root of) Eq. (70), i.e., the standard deviations are smaller. Nevertheless, it is clear that spectral averaging is a powerful method for reducing the random errors – even averaging just five spectra. A definitive bias towards larger outliers in c can be seen in Fig. 13. This is more clearly exemplified in Fig. 15, a contour-scatterplot of the c estimates versus the η_1 estimates. The horizontal and vertical lines indicate the true value of those parameters. The solid black curve is the same as shown in Fig. 8, which in turn comes from the sum of the ratios in Eq. (64) and subsequently embodied in the equation for the bias, Eq. (65). This plot show how the bias is a fundamental aspect of the problem, not an artifact of the processing methodology. Recall that the bias comes from the sum of the ratios of the true amplitude spectrum (i.e., with the true value of η_1) divided by the amplitude spectrum evaluated at a different η_1. As can be seen from Fig. 2, excepting for the lowest frequencies, the spectrum for the $\eta_1 = 19\,200$ curve is always lower than that for $\eta_1 = 20\,200$; hence, the sum will be greater than one, thus producing an overestimate of c. Alternatively, if the estimated value of η_1 is greater than the true value, the sum of the ratios will be less than one and will give an underestimate of c. This explains the biased structure for the estimates of c, as seen in Figs. 13 and 15.

A significant concern in any estimation algorithm is the identification and elimination (or mitigation) of outliers. In the results just presented, it could be seen that the overall statistical performance of the estimators is quite good, but in a real world application one needs to know if a given sample is accurate or not. This is a difficult problem in general, and even more so in this application because of the non-independence of the parameters (refer back to Figs. 1–7), as well as the significant level of random error inherent in the exponential noise. As mentioned above, the ratios of the true (in this case, simulated) spectra to the model spectra with the estimated parameters should be approximately distributed as an exponential random variable with mean one. The collection of ratios in question is taken over the set of frequencies samples for the given realization. An investigation was made into whether fitting an exponential distribution to the ratios could be used to determine the accuracy of the parameter estimates. This is a standard technique in the category of "goodness-of-fit" tests. A number of tests were employed: Anderson-Darling, Cramer-von Mises, Kolmogorov-Smirnov, Kuiper, Pearson chi-square, and the Watson U^2 test (Lindgren, 1968). Each test produces a so-called test statistic, which then leads to the probability (or "p-value") that the given data comes from the specified distribution. For each realization, the ratios were calculated and then tested as to how likely they were to come from a mean-one exponential distribution. Table 3 shows the results of this method for a specific realization. In this case, which will be discussed more thoroughly below, the p-values are close to one across the board. Unfortunately, these excellent p-values do not correspond to excellent parameter estimates. Figure 16 illustrates the results using the Anderson-Darling test, giving the p-value as a function of the c estimate for each of the 1000 realizations. The color-coding is proportional to the number of counts at that (c, p-value) grid cell. An optimal result would produce an upside-down "V" pattern (though not uniform in the number of counts), with the base of the two legs at the zero p-value axis, and the apex at the true c value and a p-value of one. That is, the higher the p-value (i.e., closer to one), the better the estimate – and vice-versa. As can be seen from the figure, the Anderson-Darling test is clearly not optimal. There is skill, but there are too many mid to low p-values associated with good c estimates, as well as some poorer c estimates with high p-values. In other words, the p-value for this test could not be used as a single criterion for identifying outliers. Figure 17 shows the same type of results for the Pearson chi-square test. The performance of this oft-used test is worse than that for the Anderson-Darling test. The Pearson chi-square test is used so frequently that a comment is warranted as to why it does not perform well in this case. As discussed in Lindgren (1968, p.486), the Pearson test is not well-suited to continuous distributions, the difficulty laying in choosing the appropriate binning strategy. The other tests, such as the Kolmogorov-Smirnov and Anderson-Darling, which use the distribution functions directly, do not have this limitation. A simple hybrid method was used as the goodness of fit metric – the maximum p-value over all the tests. The results of this method for the c parameter estimation are shown in Fig. 18. While certainly not optimal, this approach is an improvement over the individual tests. Figure 19 illustrates the same procedure, but for the η_1 estimates. In this case, there more skill than in the c estimation scenario, but as a stand-alone outlier detection method, this approach is probably not adequate. In the next section, a number of case studies are presented which will lead to a better understanding of the difficulties in the estimation and outlier identification problem.

4.2 Simulation case studies

The first case that is analyzed is realization number 64. (As an aside, a seeding method that allowed for reproducible results was used with the random number generator.) Figure 20 through Fig. 22 show the spectra, likelihood function and distribution of ratios for this realization. Since figures like these will be used to discuss other realizations, a brief description is in order. Figure 20 shows the true spectrum (black), simulated spectrum (red), and the theoretical spectrum with the estimated c and η_1 values (green). Figure 21 illustrates the likelihood function derived from the true spectrum (black), the simulated spectrum ("empirical", in red), and the spectrum with the estimated parameters (blue). Another likelihood function is plotted, (labeled "scaled"), where the true likelihood function is scaled up or down such that its minimum (at the true η_1) is shifted to equal the empirical likelihood function at the true η_1 value. Figure 22 shows a histogram of the ratios, along with a curve representing a smoothed histogram (red) and a curve which is a mean-one exponential density function (black). Table 4 gives the estimated values of c and η_1, along with the mean and standard deviation of the ratios, and a chi-square like error function computed as

$$E_\mathrm{E} = \sum_{i=1}^{P} \frac{\left[-\ln L_\mathrm{D}\left(\eta_i\right) - \left(-\ln L_\mathrm{E}\left(\eta_i\right)\right)\right]^2}{\ln L_\mathrm{E}\left(\eta_i\right)} \tag{73}$$

where, the sum is over all η values (15 000 to 25 000 km with a resolution of 10 km, i.e., $P = 1000$), $-\ln L_\mathrm{D}$ is the negative log-likelihood calculated from the data (empirical curve), and $-\ln L_\mathrm{E}$ is that derived from the estimated ("*E*") parameters. Another statistic, E_S, is calculated using the scaled ("*S*") likelihood function. Note that this statistic is not a goodness of fit metric for the fit to the spectrum, but rather for the fit to the likelihood function. The reason for this choice is that the likelihood function is more sensitive to parameter changes as is the spectrum, and that the final parameter estimates come from the likelihood function – not the spectrum.

From Table 4, it can be seen that the parameter estimates are quite poor, even though the mean and standard deviations are close to one, as one would expect from a mean-one exponential distribution. The error statistics are moderately large, and it is clear that the error statistic using the scaled likelihood function – which is almost identical to the true one – is much larger than that for the estimated one. This implies that in this case, the E_E and E_S statistics, nor the difference between them would indicate that the parameters are significantly in error. The p-values for this realization, shown in Table 3, are very high, which indicates that they are also not helpful in determining whether the parameters are outliers. This is reinforced by how well the distribution of the ratios matches the exponential curve – as seen in Fig. 22. As mentioned previously, the random errors are large, and hence the likelihood function can have undulations, which can result in a global minimum offset from the "true" minimum. It was also mentioned that this issue is especially problematic for smaller η values, where the likelihood function has a shallow incline. This is exactly what occurs with this realization, as clearly seen in Fig. 21. To investigate this further, a set of model parameters were chosen "by eye" to produce a better fit to the empirical likelihood function. This was a surrogate for a more sophisticated algorithm which might find the best fit to the empirical likelihood by varying the c and η_1 (as well as L) parameters as part of a two- or three-dimensional minimization algorithm. The results of "by eye" fit are shown in Figs. 23 and 24. The fitted parameters were chosen after fixing η_1 at its the true value; and as can be seen in the figures, these parameter choices do produce a better fit than the estimated parameters. The error statistic for the fit, E_F, is 81.6; whereas E_E and E_S are 100.0 and 158.1, respectively. A better fit can be obtained by lowering η_1 to 19 800 and raising c to 4.25×10^{-9}, giving $E_\mathrm{F} = 31.3$. This gives hope for more accurate parameter estimation by using a more sophisticated minimization methods, i.e., estimating L in addition to c and η_1.

The next case that was analyzed is realization 308. For this realization, the parameter estimates were also significantly in error, although in the opposite fashion – the c value was underestimated (2.1×10^{-9}) and the η_1 value was overestimated (22 250). As with realization 64, the p-values were very high. The spectra, likelihood function and ratio distributions are shown in Figs. 25–27. As seen by the green curve in Fig. 26, the fit of the estimated likelihood function to the empirical one is quite good, with $E_\mathrm{E} = 6.2$ (and $E_\mathrm{S} = 31.8$). This occurs even with the poor parameter estimates. In this realization, the likelihood function is somewhat flat, even out to large η values. Hence, the global minimum for the likelihood function ended up at a large η value. However, by fixing $\eta_1 = 20\,200$ and changing c (3.36×10^{-9}) and L (2.5), an even better fit ($E_\mathrm{F} = 1.0$) was obtained (blue curve). This is far superior to using the initial parameter estimates. Since the values for c and η_1 are more important for practical applications, the error induced by lowering the value for L, in exchange for more accurate c and η_1 estimates is acceptable. As with realization 64, there are no clear indications from the p-values and E_E metric that the original estimates for c and η_1 are in error.

The next two cases that were examined, realizations 356 and 177, had low p-values. The original estimates for realization 356 were, $c = 9.1 \times 10^{-9}$ and $\eta_1 = 17\,320$, and the error statistics were $E_\mathrm{E} = 284.2$, and $E_\mathrm{S} = 37.5$. As with realizations 64 and 308, using the true value for η_1 and adjusting c in a minor fashion (to 4.32×10^{-9}) and L in a more significant way (to 9), produced an excellent fit to the empirical likelihood function ($E_F = 10.3$). This can also be seen in Figs. 28 and 29. The distribution of the ratios for realization 356 is shown in Fig. 30. The distribution of ratios for realization 177 is shown in Fig. 31. Comparing the distribution plots for these two realizations, a possible reason for the low p-values is visible: the number of far outliers, e.g., values greater than five or six. Comparing these distribution plots with those for realizations that have high p-values, e.g., 64 and 308, a subtle trend towards more far outliers can be seen in the low p-value cases. A more thorough investigation is needed to see if this holds over a large number of realizations. The last case considered is realization 127. This is an interesting situation, in that the parameter estimates were close to perfect and yet the fit of the estimated likelihood function to the empirical one is not good ($E_E = 45.4$). By increasing L to 15 and decreasing c to 3.96×10^{-9}, a better fit to the likelihood function was obtained ($E_F = 7.7$). This case reinforces the concept of how the random errors in the data can produce wide variation in the shapes of the likelihood functions, and that these variations can produce either good or bad parameter estimates.

4.3 Weighting and spectral averaging

As mentioned above, two techniques that can improve the parameter estimation are employing a weighting function in calculating the log-likelihood function and spectral averaging. Figure 33 shows benefit in using a weighting function. The red and brown curves are the un-weighted empirical and estimated likelihood curves, respectively, for realization 64. Recall that the parameter estimates for this case were poor ($c = 8.4 \times 10^{-9}$ and $\eta_1 = 17\,210$). Since the η_1 estimate is on the low end of the η-range, the use of a weighting function should improve the estimates. As can be seen from the figure (blue and green curves for the weighted empirical and estimated likelihood curves, respectively), the new estimates are superior to the un-weighted method: $c = 3.98 \times 10^{-9}$ and $\eta_1 = 20\,150$. Next, we turn to spectral averaging. A small number of realizations are averaged (5) to show the benefits of this method. Of course, for a GNSS-LEO occultation geometry, the vertical extent of the atmosphere covered over the period required to average five spectra can be large. Running averages could be used, but then the samples would not be independent and the effect of averaging on the variance – as given by Eq. (69) – would be lessened. Hence, a combination of averaging and weighting, along with a multi-dimensional parameter estimation method as described above would be required. For now, consider the use of averaging by itself with simulated data. Figure 34 illustrates the benefit of averaging on reducing the random errors. The blue curve is the un-averaged spectrum from realization 127, and is merely shown as a reference – the five spectra used in the averaging do not include that realization. The red curve in this figure is the averaged spectrum and the black curve is the true spectrum. It can be seen that the averaged spectrum is better matched to the true spectrum compared to an un-averaged one. One would then expect the likelihood function derived from the averaged spectrum to also be closer to the true likelihood function. Indeed, Fig. 35 bears this out. Figures 36–38, are the spectrum, likelihood function and ratio distribution plots, respectively, for another averaged spectrum. This case was chosen because it resulted in excellent parameter estimates and p-values. Recall the discussion above regarding how the distribution function for the ratios becomes a gamma distribution with parameters $\alpha = M$ and $\beta = 1/M$, where M is the number of spectra going into the average (here, 5). This theoretical development holds true, as can be seen in Fig. 38. Another set of five realizations were chosen to illustrate a situation where the parameter estimates and the p-values are not as good, as shown in Figs. 39–41.

5 GPS-COSMIC occultation analysis

The theory, techniques and observations presented in the previous sections would be useless if they did not apply to real data. In this section, an analysis of two case studies from GPS-COSMIC occultations is presented. These cases occurred in relative (space and time) proximity to the Air France 447 accident that occurred on 1 June 2009. These results are not meant to provide any insight into the cause of the accident – these cases were selected merely as a matter of interest: it is known that there was vigorous convective activity in the region, as well as turbulence reports from the Air France pilots and other aircraft in the vicinity. In each case, a 500-sample analysis window was selected and processed using the same methodologies as used with the simulated data. There is one difference, however. A trend was removed from the time series data prior to the analysis. Figure 42 shows the amplitude time series over the course of occultation 2 (arbitrary nomenclature). The black curve is the raw data, the red curve shows the trend, and the two vertical dashed blue lines delineate the analysis window. It is possible that this window corresponds to the tropopause, or perhaps at the upper boundary between the thunderstorm and the overlying air. This conjecture is based on the fact the data just prior to this window are fairly smooth, and then the fluctuations become quite large. The trend was computed via a running median filter with a width of 2001 points, or approximately 40 s. The appropriateness of the filter window was checked by verifying that the residuals had a mean that was close to zero. Figure 43 shows the spectra of the data (red) and the spectra using the estimated parameters ($c = 5.1 \times 10^{-10}$, $\eta_1 = 19\,010$, $L = 7.5$ and $Q = 1.5 \times 10^{-5}$). The likelihood functions for the weighted and un-weighted methods are presented in Fig. 44. The red (blue) curve is the empirical un-weighted (weighted) function and the black (green) curve is that for the estimated un-weighted (weighted) likelihood function. For the un-weighted case, $E_\text{E} = 31.6$, which is a moderate value. Figure 45 illustrates the distribution of ratios. From these figures, it can be seen that the characteristics of the real data are similar to those of the simulated cases (e.g., realization 64). Table 5 shows the p-values for this case. These values would be expected by an examination of Fig. 45.

The time series data for occultation 1 is shown in Fig. 46. This is similar to occultation 2, in that the data in the window may be representative of a boundary between smoother air above and very disturbed air below. It can be seen that there are significant fluctuations within the window. Figure 47 shows the spectra for the data (red), the spectra derived from the estimated parameters (black), and that using a set of "by-eye" fitted parameters (blue). The spectrum of the data shows features that were not seen in the simulated data. For example, the "hump" around 5 Hz, and some organized structures at higher frequencies (e.g., around 7 and 9 Hz). Clearly, the spectral points around 5 Hz. are not independent, and are most likely related to distinct oscillations in the time series. In fact, if we look at the time series over the analysis window (Fig. 48), there is a significant ramp in the data just past 54 s. Given the steady rise in magnitude, this is probably not a spike due to a data artifact, but it could come from a sharply layered atmospheric structure. Figure 49 shows the de-trended phase data from the same window. A somewhat similar structure as with the amplitude (without the oscillations) can be seen between 54 and 56 s. Note that the de-trending used with the phase data was very different than that used with the amplitude data. A polynomial fit over an extended time segment, centered at the analysis window was employed. For this example, the fit was performed over a window extending 150 points before and after the analysis window. For approximately 1.5 s past the large ramp in the amplitude data, an organized oscillation can be seen. The period of the oscillation appears to be constant, while the magnitude is decreasing. The source of these oscillations is unknown, but their period is approximately 1/4 s, which gives a frequency of 4 Hz. Hence, it is probable that these oscillations are the source of the hump in the spectrum. It is interesting to note that there are also oscillations in the likelihood function, seen in the empirical (red) curves in Figs. 50 and 51. Since the likelihood function is derived from the spectrum, not the time series, this is an intriguing artifact. Not only is this an artifact, but one of the oscillations happens to be the global minimum, skewing the parameter estimation (see the green curve in these figures). A "by eye" fit was performed (blue curves) which provided far superior parameter estimates – or at least a better fit to the empirical likelihood function – since the true values are unknown. The estimated and fitted error statistics are $E_E = 299.2$ and $E_F = 7.7$, respectively. The associated parameter estimates were $(c, \eta_1) = (2.76 \times 10^{-9}, 17\,730)$ and $(1.37 \times 10^{-9}, 20\,800)$, respectively. It is encouraging that even with the data quality issues, reasonable parameter estimates can be obtained with fits to the likelihood function – just as was seen with the simulated data. The ratios for this occultation also contain the artifacts of the oscillations. In fact, these are directly related to the hump around 5 Hz., as those values – being much larger than the model spectrum, in turn produce large ratios. This can be seen in Fig. 52, (where it should be noted that the horizontal scale has been enlarged over those used in the other distribution plots), and especially in Fig. 53, which shows the ratios as a function of frequency. The large values around 5 Hz are the outliers.

6 Conclusions

In this paper, a overview of the derivation used to produce the model spectrum was presented. This derivation started from the Helmholtz wave equation, and using a reasonable set of assumptions, resulted in the model spectrum, Eq. (43), and its mid-point approximation, Eq. (45). This latter model was used in the subsequent analysis. In the next section, a simplified parameter estimation methodology was presented, followed by a discussion of the statistical properties of the estimators. A detailed study using simulated data was presented after the theoretical discussions. A number of metrics were examined to evaluate the accuracy of the estimates. It was found that the use of two parameters, the turbulence intensity and the location of the turbulence along the line of sight, produced relatively accurate estimates. In this instance, the term “accurate” refers to the global statistics over all the simulated realizations. In a practical application, one would like to have accurate estimates for each measurement, or at least a notion as to when the estimates are unreliable. No single metric that could satisfy the latter was found, but it was seen that with the addition of a third parameter – the turbulence length scale – quite accurate parameter estimates could be made for individual realizations. Since the simple parameter estimation technique used the global minimum of the log-likelihood function, random errors in the spectrum could result in significant errors when determining the location of the turbulence. An important step in improving the parameter estimation was fitting the model-based likelihood function to the empirical one. In addition to incorporating the third parameter into the fitting, a weighting function was introduced into the likelihood estimation methodology. This not only allowed for the elimination of the most egregious outliers, but it also lead to improved parameter estimates from the data interior to the weighting function's effective region. Finally, it was shown that spectral averaging greatly improved parameter estimation. This is due to damping the effect of the random errors in the spectra. The smaller errors then propagate through the parameter estimation resulting in more accurate estimates. The methods developed for the analysis of the simulated data was then applied to the analysis of real occultation data. While only the results from two cases were presented, it could be seen that the general characteristics seen in the simulated data were also seen in the real data – which is encouraging. On the other hand, the simulation did not make use of a model that allowed for anisotropic turbulence, nor did it reflect data quality issues, both of which will be seen in real data.

Future work includes the implementation of a three-parameter estimation algorithm and a more thorough analysis of real occultation data. This is especially needed for phase data. Some analysis has been performed with simulated and real phase data, with encouraging results, but not to the extent presented here with the amplitude data. There are distinct issues regarding trend removal with the phase time series. A local polynomial fitting method was discussed briefly; however, the frequency content in the data resulting from polynomial fitting is highly dependent on the order of the polynomial used and the window over which the fit is performed. This indicates that a more robust methodology needs to be developed.

Overall, the results of these studies are quite encouraging and give confidence that accurate turbulence information can be derived from GNSS occultation data.

Acknowledgements. Support for this project has been provided by the NASA GNSS Science Team, NASA Grant #NNX08AH68G, Technical Officer John LaBrecque, NASA Headquarters.

References

Conker, R. S., Bakry El-Arini, M., Hegarty, C. J., and Hsiao, T.: Modeling the effects of ionospheric scintillation of GPS/Satellite-based Augmentation System availability, Radio Sci., 38(1), 1001, doi:10.1029/2000RS002604, 2003.

Cornman, L. B., Frehlich, R., and Praskovskaya, E.: The detection of upper-level turbulence via GPS occultation methods, in: Occultations for Probing Atmosphere and Climate, editec by: Kirchengast, G., Foelsche, U., and Steiner, A. K., Springer-Verlag, Berlin, Heidelberg, 2004.

Cornman, L. B., Weekley, A., Goodrich, R. K., and Frehlich, E.: Using airborne GNSS receivers to detect atmospheric turbulence, in: New Horizons in Occultation Research, edited by: Steiner, A. K., Pirscher, B., Foelsche, U., and Kirchengast, G., Springer-Verlag, Berlin, Heidelberg, 2009.

Evans, G., Blackledge, J., and Yardley, P.: Analytical Methods for Partial Differential Equations, Springer, London, 2000.

Freund, J. E.: Mathematical Statistics, 5th edition, Prentice-Hall, New Jersey, 658 pp., 1992.

Ganguly, S., Jovancevic, A., Brown, A., Kirchner, M., Zigic, S., Beach, T., and Groves, K. M.: Ionospheric scintillation monitoring and mitigation using a software GPS receiver, Radio Sci., 39, RS1S21, doi:10.1029/2002RS002812, 2004.

Gorbunov, M. E. and Kirchengast, G.: Processing X/K band radio occultation data in the presence of turbulence, Radio Sci., 40, RS6001, doi:10.1029/2005RS003263, 2005.

Gurvich, A. S. and Chunchuzov, I. P.: Parameters of the fine density structure in the stratosphere obtained from spacecraft observations of stellar scintillations, J. Geophys. Res., 108(D5), 4166, doi:10.1029/2002JD002281, 2003.

Hajj, G. A., Ibanez-Meier, R., Kursinski, E. R., and Romans, L. J.: Imaging the ionosphere with the Global Positioning System, Int. J. Imag. Syst. Tech., 5, 174–184, 2000.

Ishimaru, A.: Wave propagation and scattering in random media, IEEE Press, New York, 574 pp., 1997

Kristensen, L., Lenschow, D. H., Kirkegaard, P., and Courtney, M.: The spectral velocity tensor for homogeneous boundary-layer turbulence, Bound-Lay Meteorol, 47, 149–193, 1989.

Kunitsyn, V. E. and Tereshchenko, E. D.: Determination of the turbulent spectrum in the ionosphere by a tomographic method, J. Atmos. Sol.-Terr. Phy., 54(10), 1275–1282, 1992.

Lindgren, B.: Statistical Theory, 3rd edition, MacMillan Publishing Co., Inc. New York, New York, 1968.

Secan, J. A., Bussey, R. M., Fremouw, E. J., and Basu, S.: High-latitude upgrade to the Wideband ionospheric scintillation model, Radio Sci., 32(4), 1567–1574, 1997.

Tatarski, V. I.: The Effects of the turbulent Atmosphere on Wave Propagation (translated from Russian by the Israel Program for Scientific Translations Ltd, ISBN 0 7065 0680 4) reproduced by National Technical Information Service, US Department of Commerce, Springfield, Va., 1971.

Tereshchenko, E. D., Kozlova, M. O., Kunitsyn, V. E., and Andreeva, E. S.: Statistical tomography of sub kilometer irregularities in the high-latitude ionosphere, Radio Sci., 39, RS1S35, doi:10.1029/2002RS002829, 2004.

Yeh, K. C. and Liu, C.-H.: Radio wave scintillations in the ionosphere, Proceedings IEEE, 70, 4, 1982.

Table 1. Statistics for maximum likelihood estimates of $C_n^2 \Delta\eta$.

$C_n^2 \Delta\eta$	Median ($\times 10^{-9}$)	STD ($\times 10^{-9}$)	40–60 Quantile Range	30–70 Quantile Range	20–80 Quantile Range	10–90 Quantile Range
Basic	3.98	0.90	0.31	0.67	1.13	2.00
Weighted	4.01	0.70	0.29	0.60	0.96	1.64
Spectral Average	4.00	0.24	0.09	0.18	0.32	0.50
Weighted, Spectral Average	4.00	0.22	0.08	0.18	0.29	0.48

Table 2. Statistics for maximum likelihood estimates of η_1.

η_1 (km)	Median	STD	40–60 Quantile Range	30–70 Quantile Range	20–80 Quantile Range	10–90 Quantile Range
Basic	20 200	903	115	400	1010	2045
Weighted	20 190	653	90	360	845	1560
Spectral Average	20 200	197	10	40	120	280
Weighted, Spectral Average	20 200	176	30	60	100	270

Table 3. Probability distribution tests: Realization 64.

Test	Statistic	P-Value
Anderson-Darling	0.196	0.992
Cramer-von Mises	0.023	0.993
Kolomogorov-Smirnov	0.022	0.999
Kuiper	0.044	0.996
Pearson χ^2	9.323	0.952
Watson U^2	0.023	0.971

Table 4. Parameter estimates and statistical measures for realization number 64.

Realization Number	η_1	$C_n^2 \Delta\eta$	Mean of Ratios	STD of Ratios	Log-Likelihood Error Statistic	Log-Likelihood Error Statistic Scaled
64	17210	8.39×10^{-9}	1.01	1.03	100	159

Table 5. Probability distribution tests for COSMIC occultation 2.

Test	Statistic	P-Value
Anderson-Darling	0.781	0.495
Cramer-von Mises	0.094	0.617
Kolomogorov-Smirnov	0.041	0.770
Kuiper	0.069	0.666
Pearson χ^2	13.713	0.748
Watson U^2	0.064	0.544

AMTD
4, 3401–3497, 2011

Title Page
Abstract Introduction
Conclusions References
Tables Figures
|◀ ▶|
◀ ▶
Back Close
Full Screen / Esc
Printer-friendly Version
Interactive Discussion

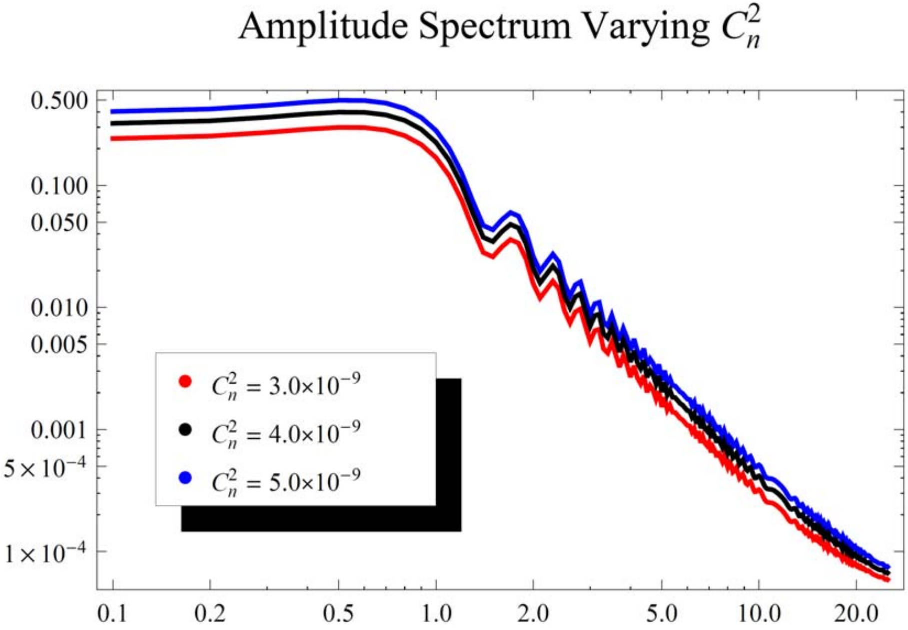

Fig. 1. Amplitude frequency spectrum (in Hz) with varying turbulence intensity values.

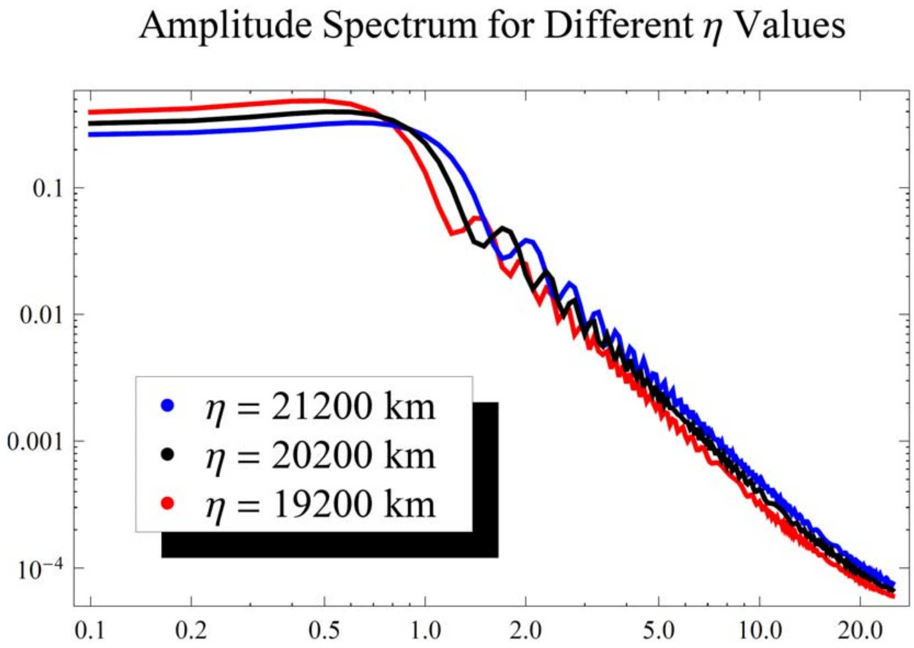

Fig. 2. Amplitude frequency spectrum (in Hz) with varying turbulence location values.

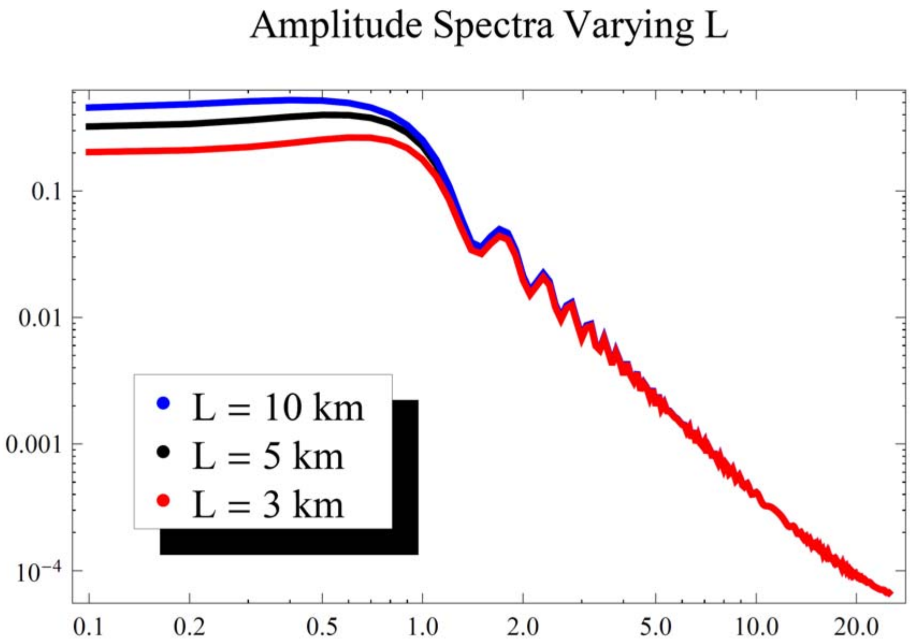

Fig. 3. Amplitude frequency spectrum (in Hz) varying turbulence length scale.

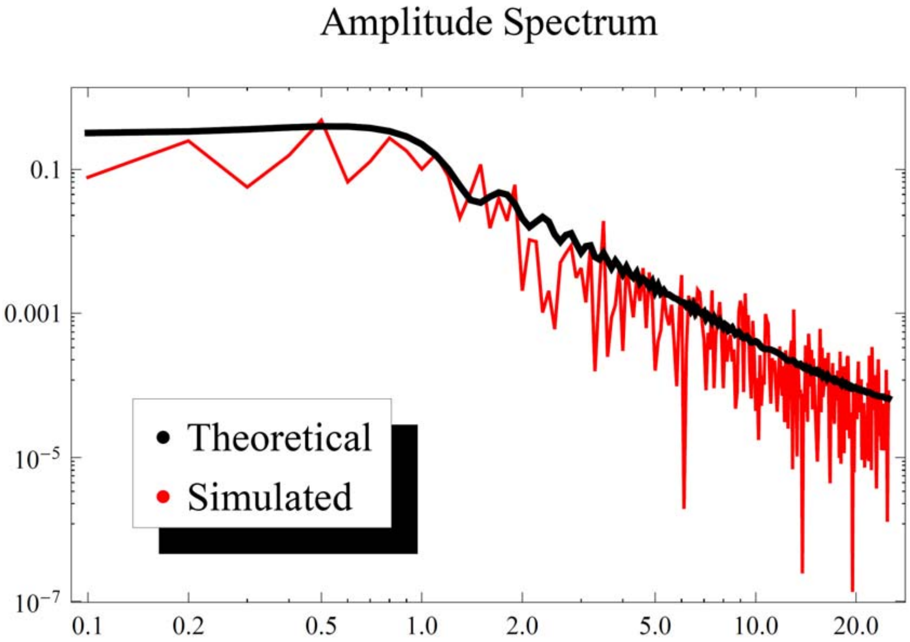

Fig. 4. Amplitude frequency spectrum (in Hz) for theoretical and simulated case.

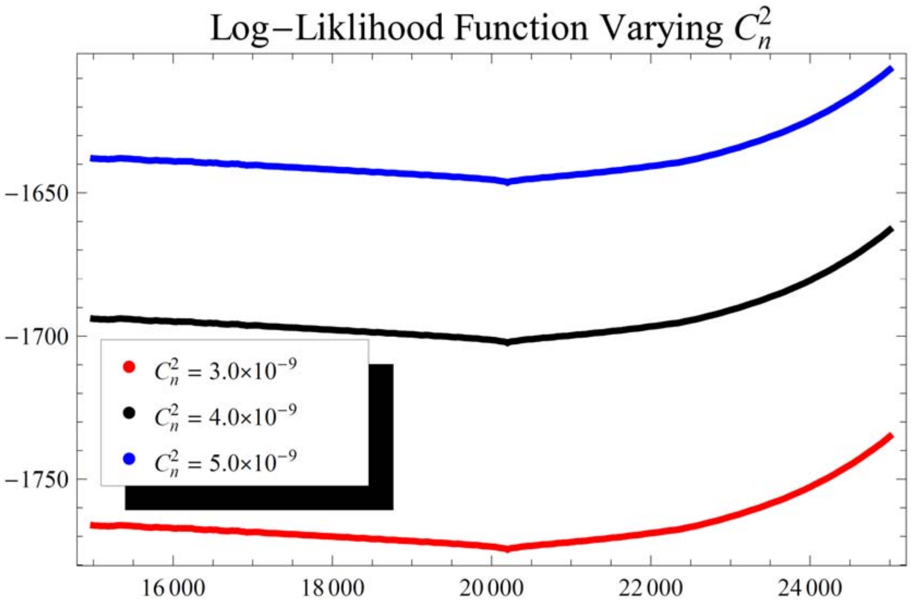

Fig. 5. Negative Log-Likelihood function as a function of η_1 in km, with varying turbulence intensity values.

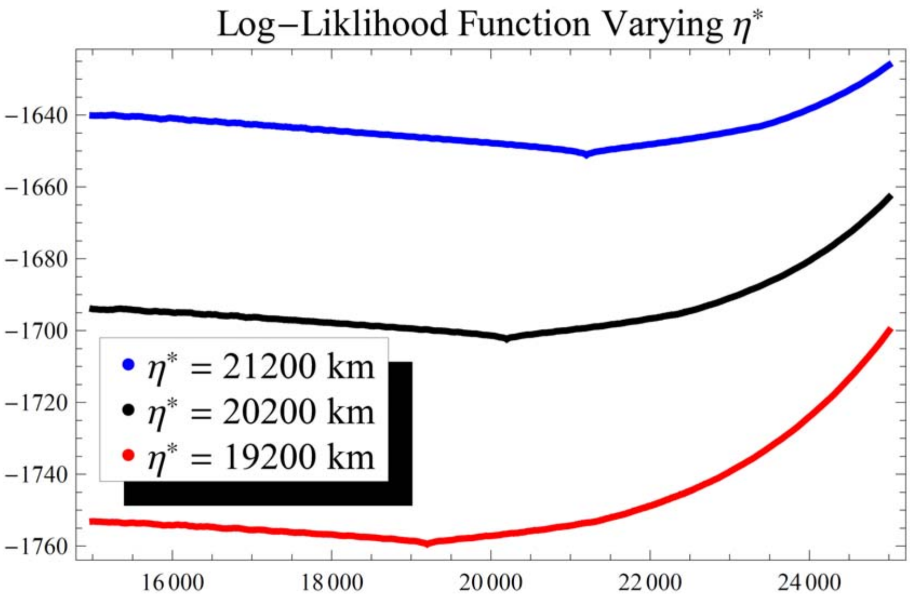

Fig. 6. Negative Log-Likelihood function as a function of η_1 in km, with varying turbulence location.

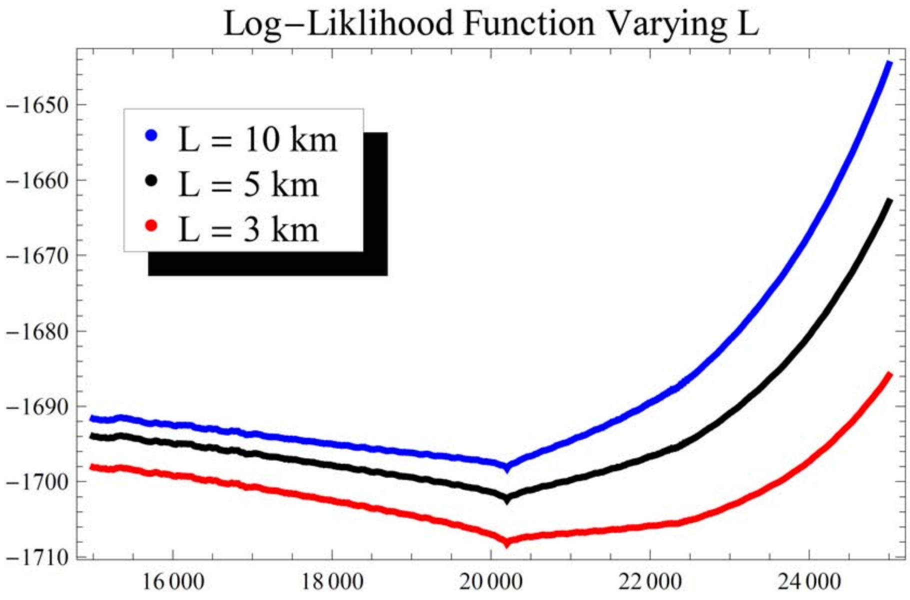

Fig. 7. Negative LogLikelihood function as a function of η_1 in km, for varying turbulence length scale.

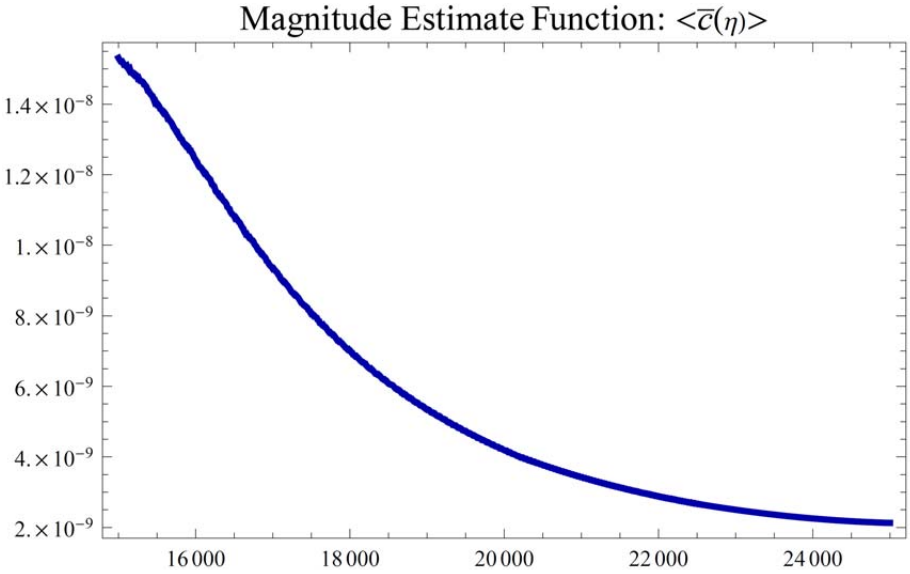

Fig. 8. Plot of Eq. (54) (and Eq. 64), as a function of η_1 in km.

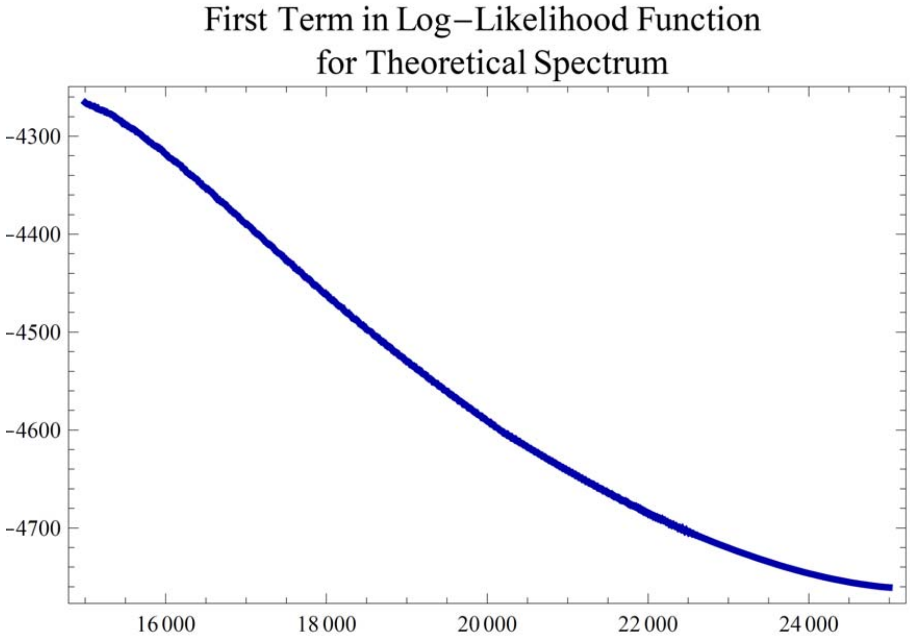

Fig. 9. First term in Eq. (55), as a function of η_1 in km.

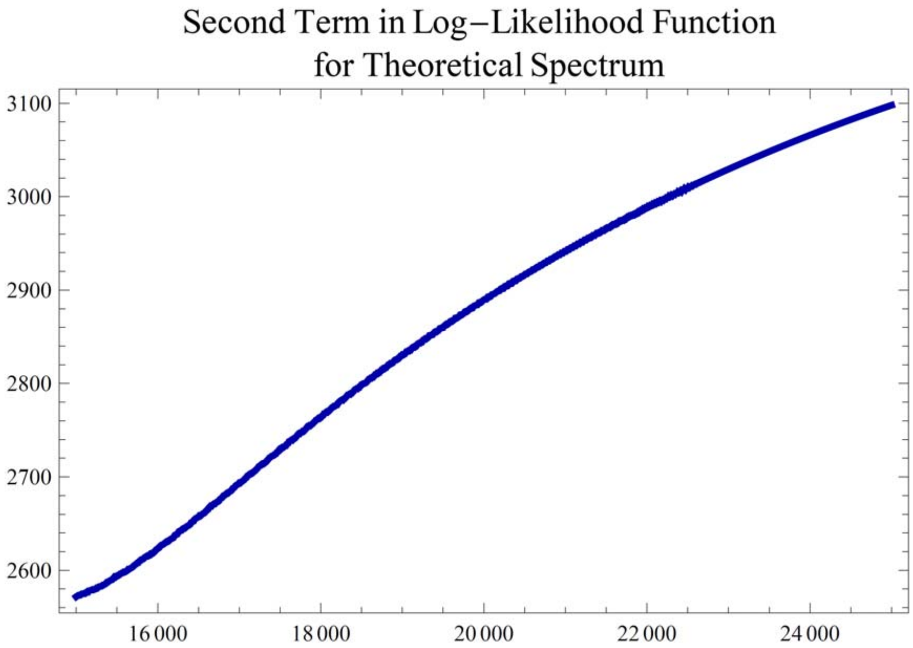

Fig. 10. Second term in Eq. (55), as a function of η_1 in km.

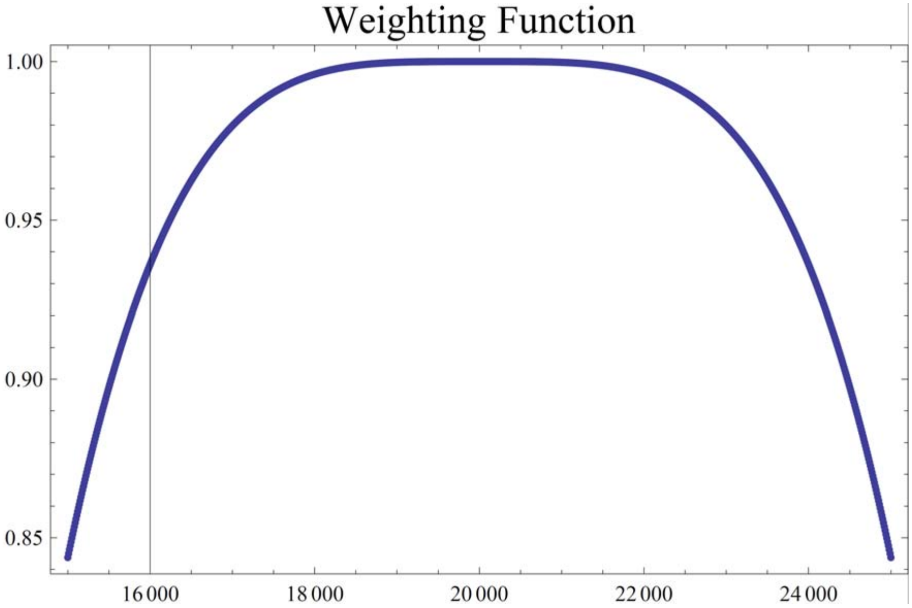

Fig. 11. Weighing function for log-likelihood function as a function of η_1 in km.

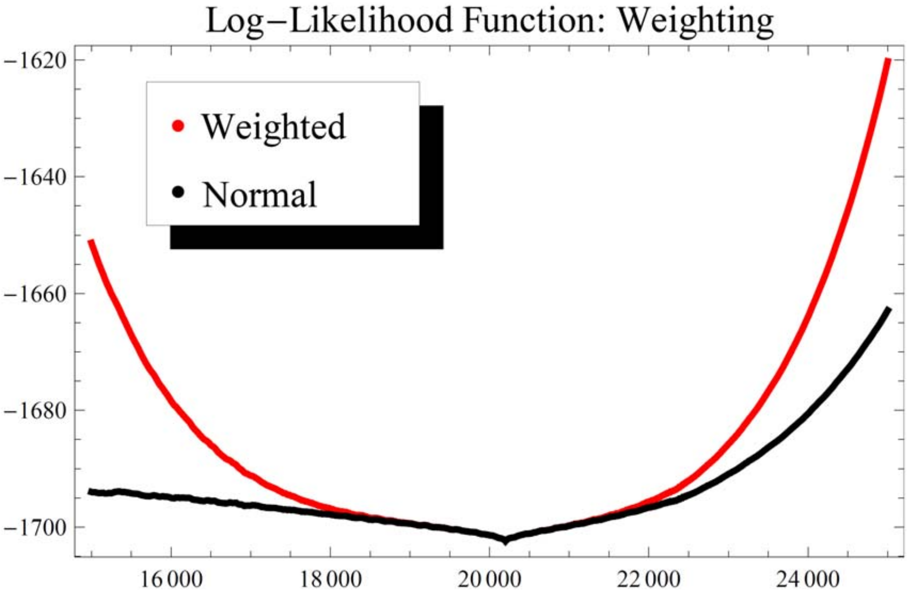

Fig. 12. The effect of the weighting function on the log-likelihood function as a function of η_1 in km.

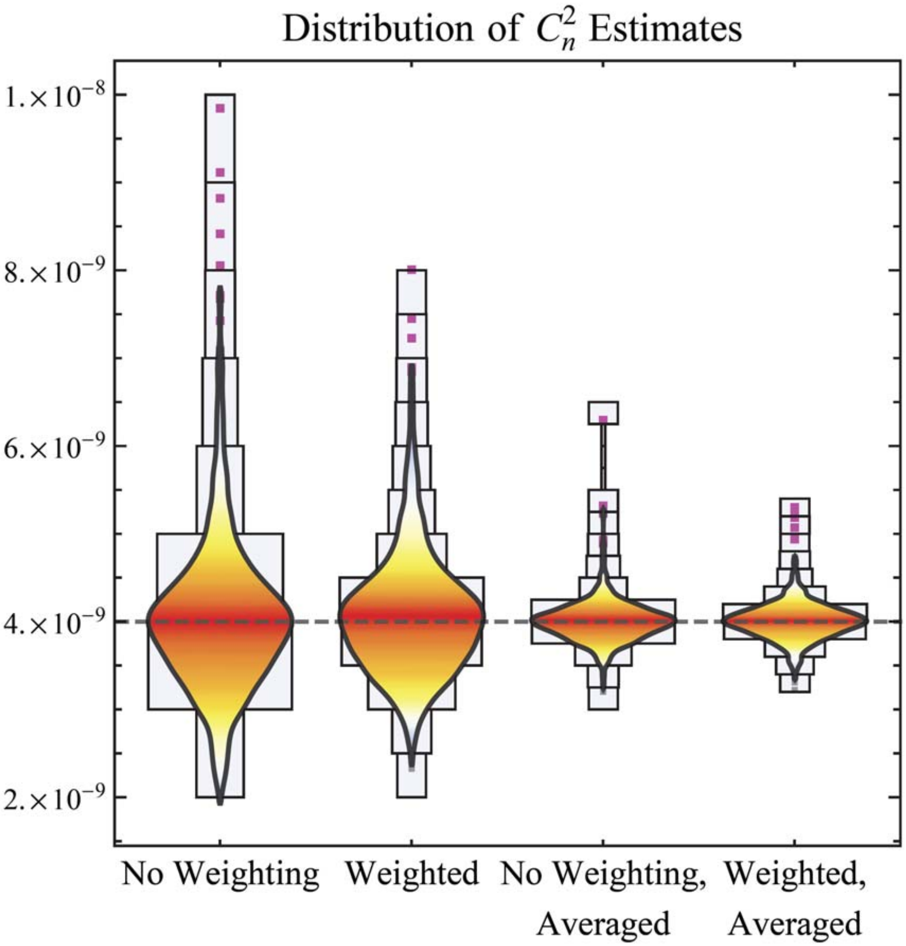

Fig. 13. Distribution of $C_n^2\Delta\eta$ estimates over 1000 realization. The dashed horizontal line is the true value.

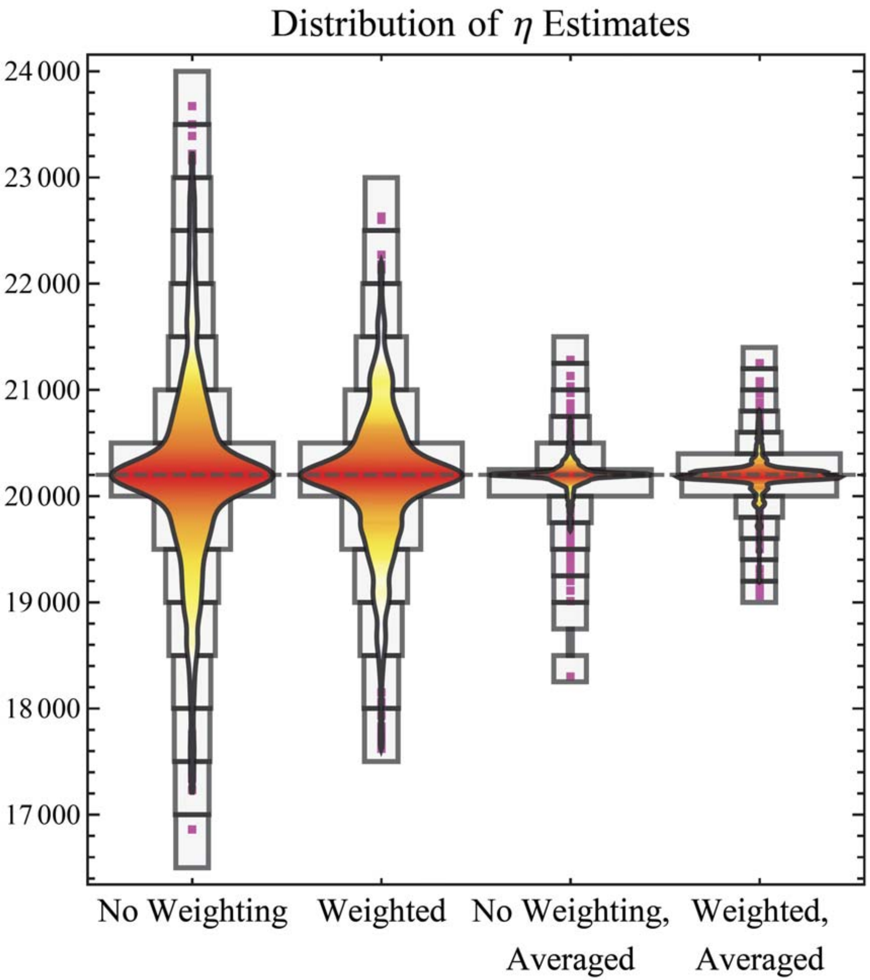

Fig. 14. Distribution of η_1 estimates. The dashed horizontal line indicates the true value.

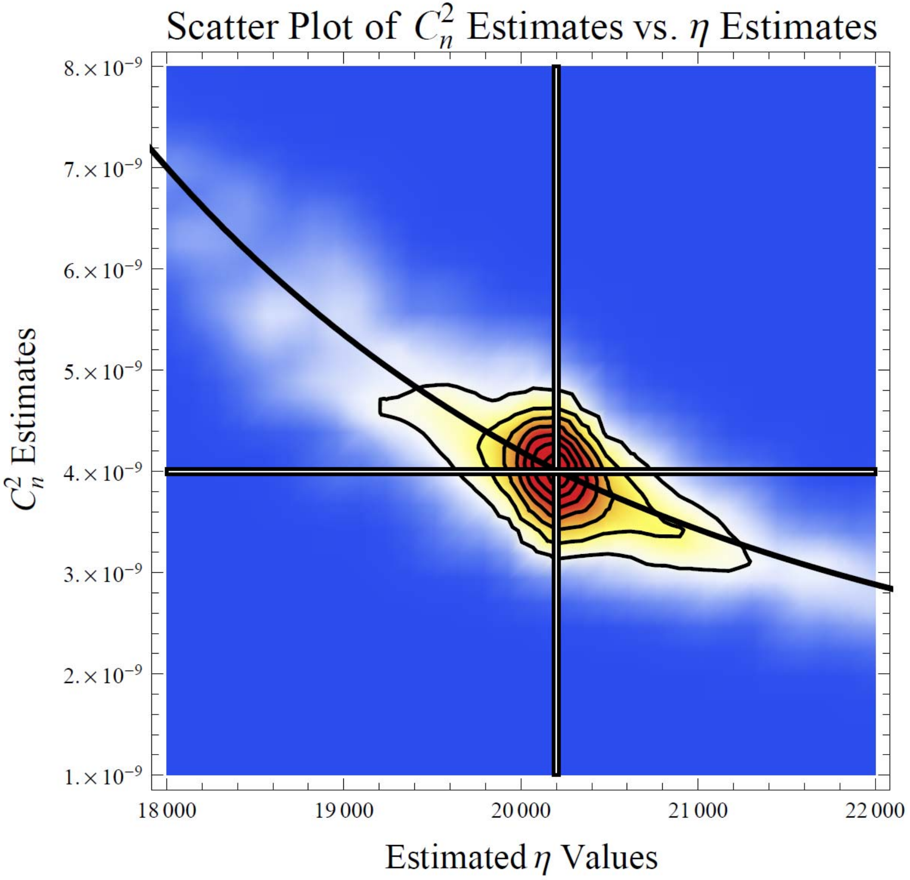

Fig. 15. Contour-scatterplot of $C_n^2 \Delta\eta$ estimates versus η_1 estimates. The horizontal and vertical lines indicate the true value values for those parameters, respectively. The solid black curve is that from Fig. 8.

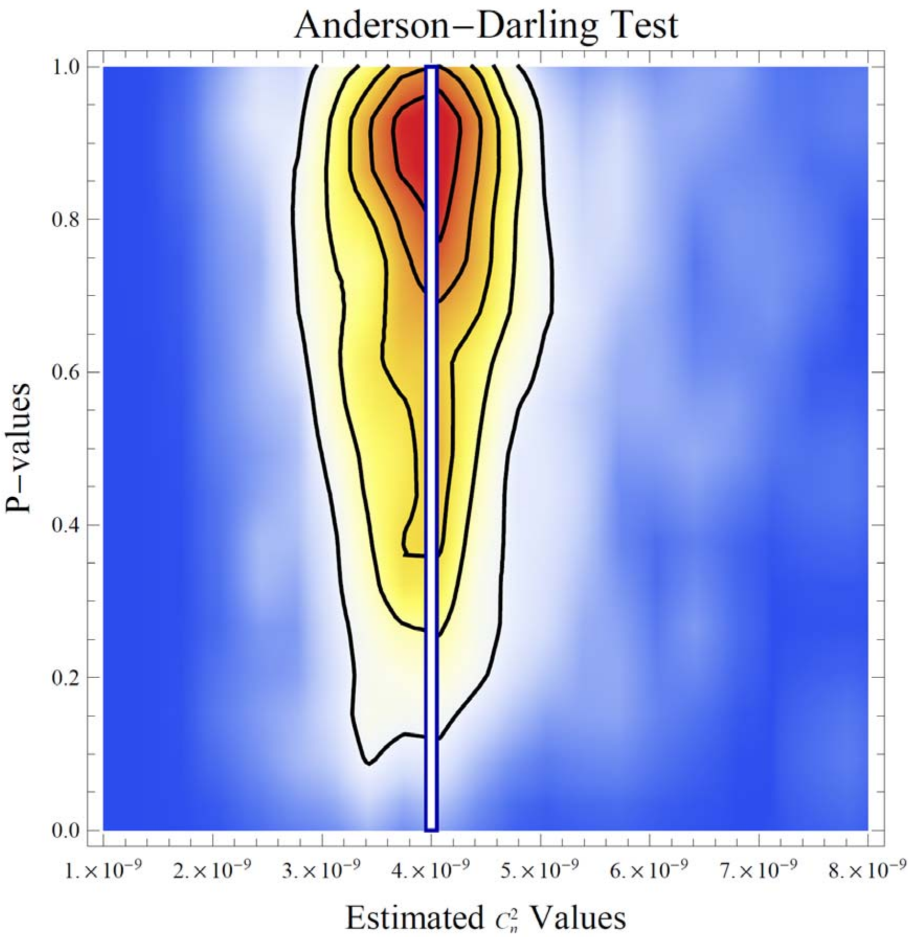

Fig. 16. Probability values for the Anderson-Darling distribution test.

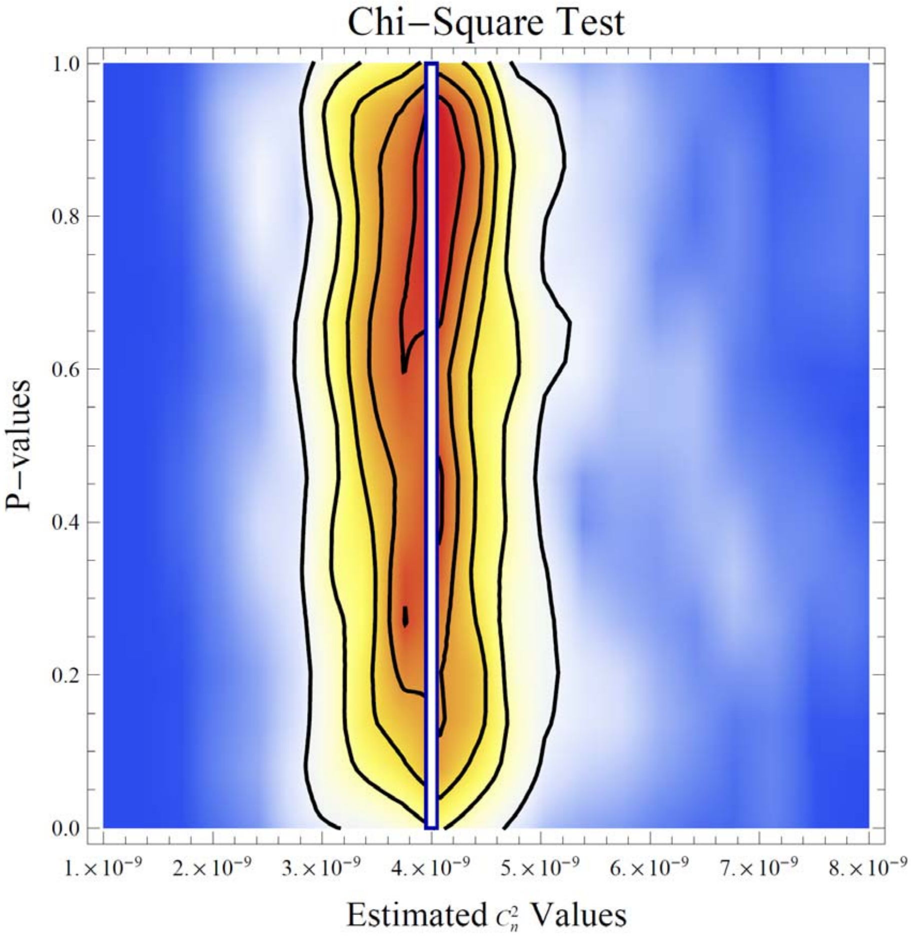

Fig. 17. Probability values as a function of $C_n^2 \Delta\eta$ estimates: Chi-square test.

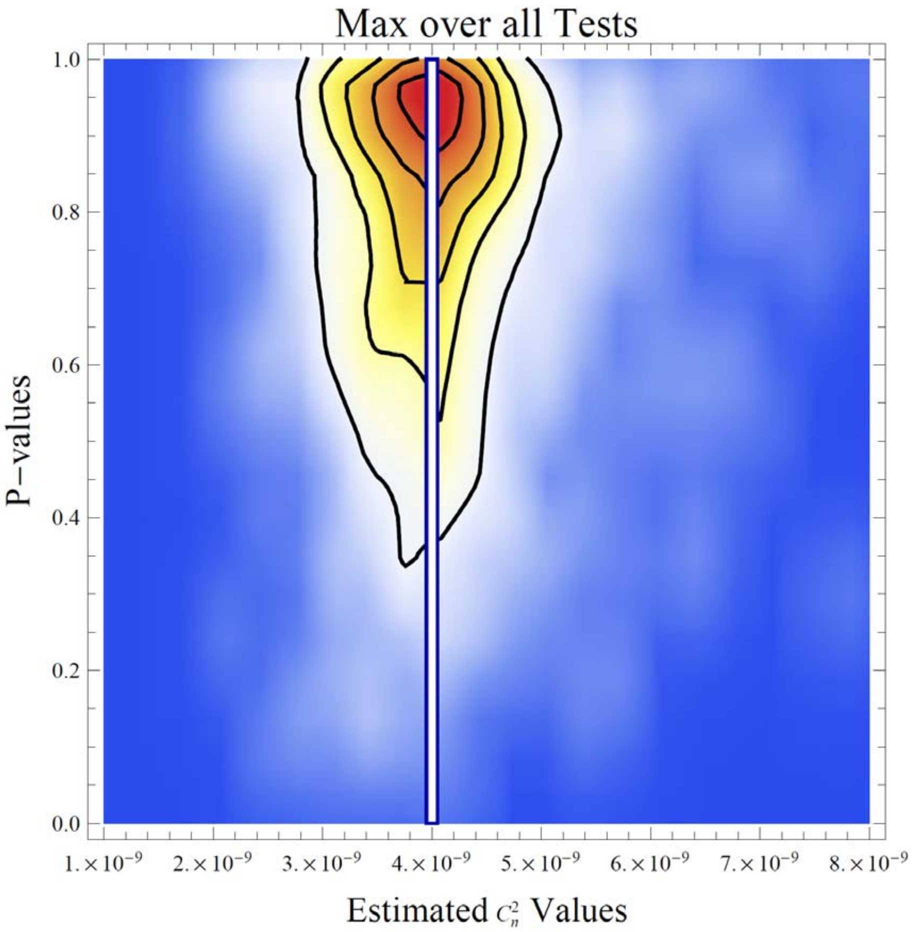

Fig. 18. Probability values as a function of $C_n^2 \Delta\eta$ estimates: maximum over all tests.

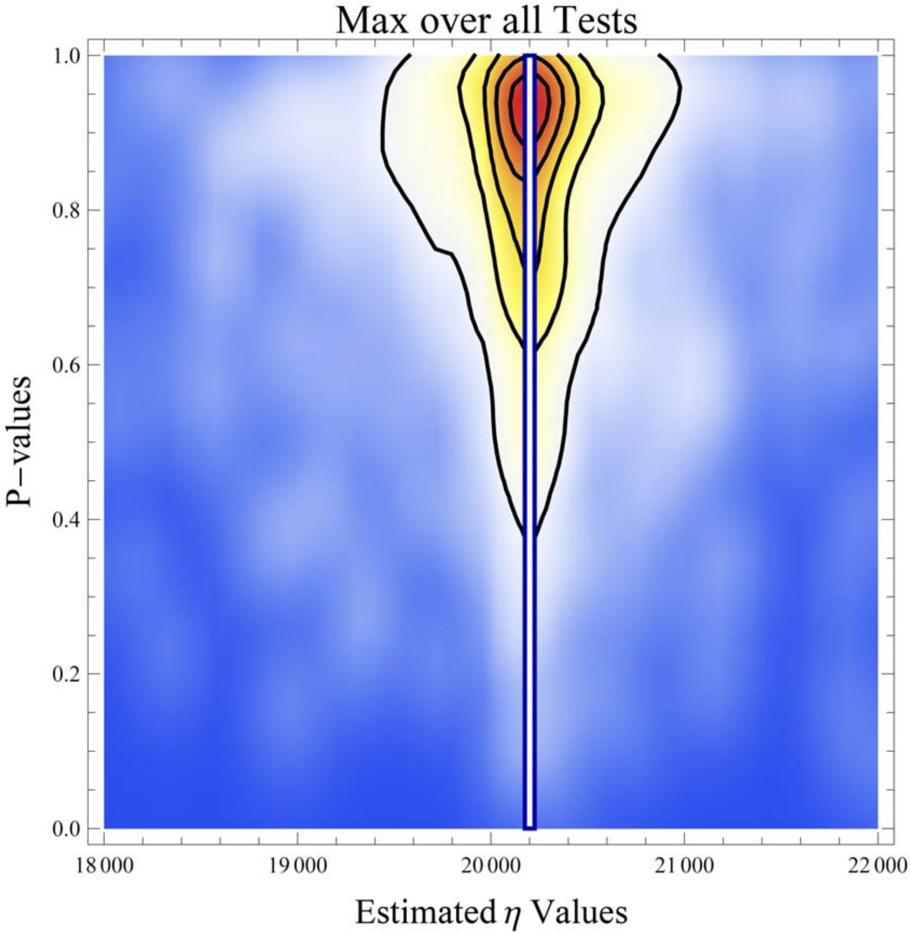

Fig. 19. Probability values as a function of η_1 estimates: maximum over all tests.

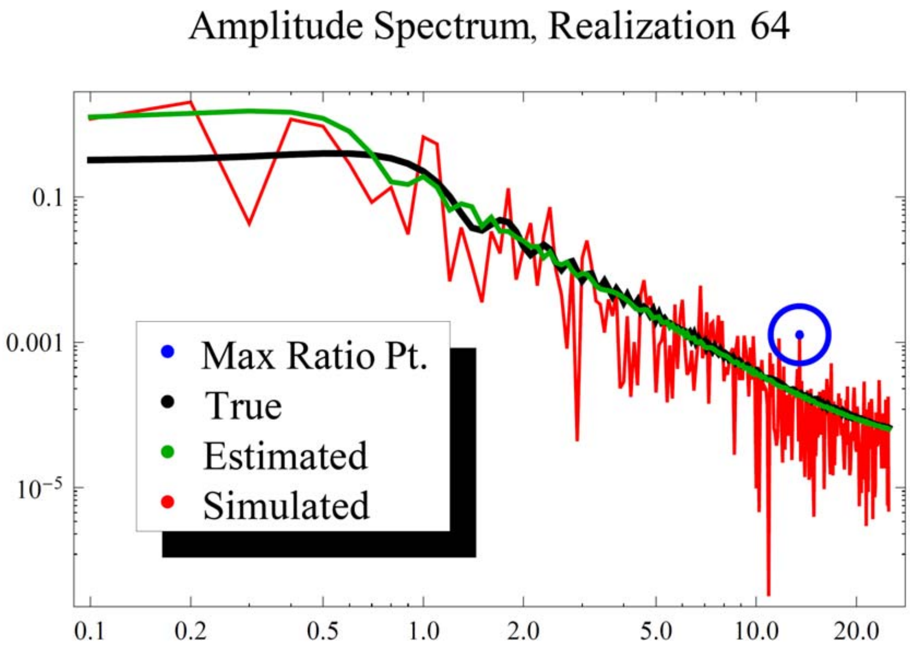

Fig. 20. Amplitude frequency spectrum (in Hz) for realization number 64, showing the simulated, true, and estimated spectra.

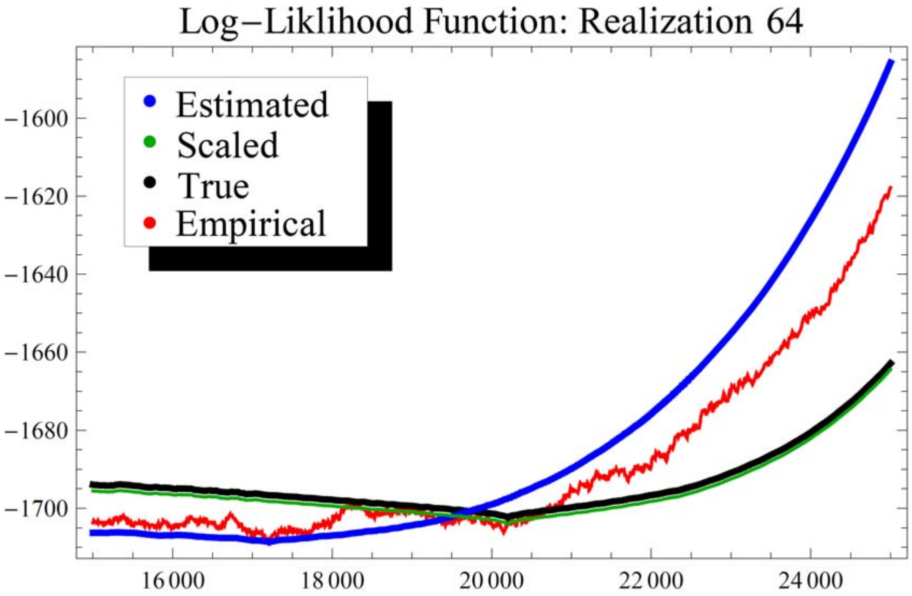

Fig. 21. Negative log-likelihood functions as a function of η_1 in km, for realization number 64.

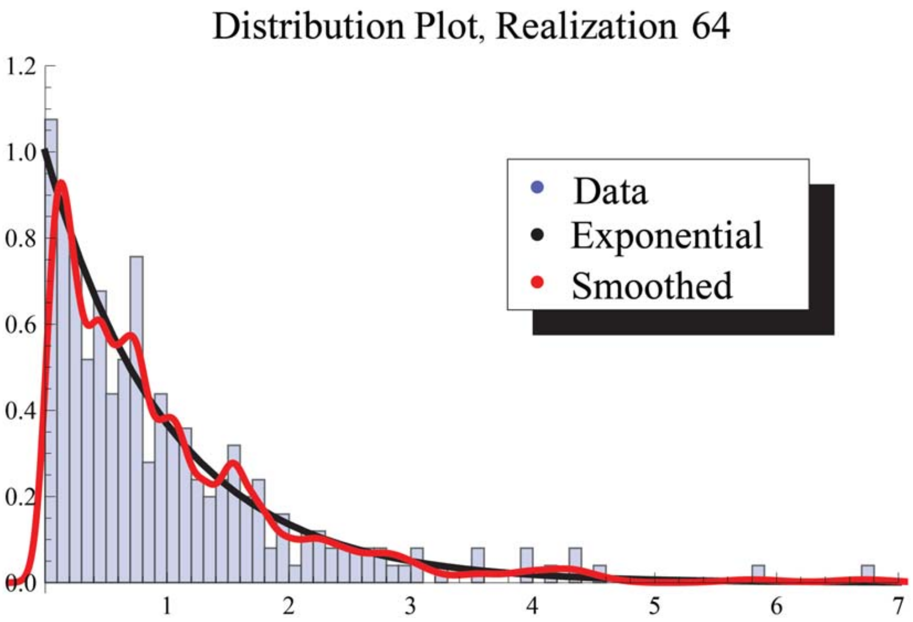

Fig. 22. Distributions plots of the ratios in Eq. (63), for realization number 65.

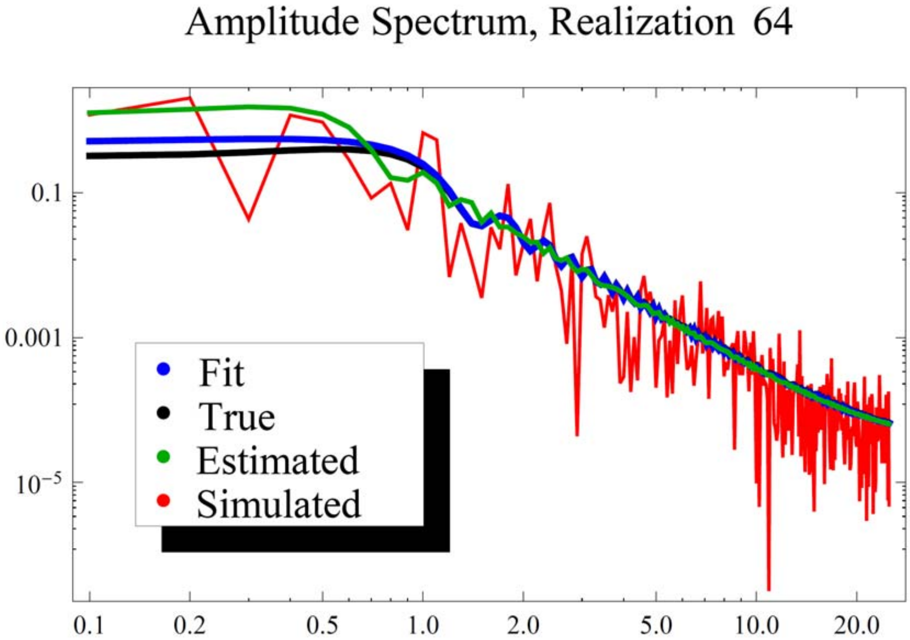

Fig. 23. Amplitude frequency spectrum (in Hz) for realization 64, showing fit ($\eta = 20\,200$, $L = 5$ km, and $C_n^2 \Delta\eta = 3.84 \times 10^{-9}$), compared to estimated ($\eta = 17\,210$ km, $L = 5$ km, and $C_n^2 \Delta\eta = 8.4 \times 10^{-9}$).

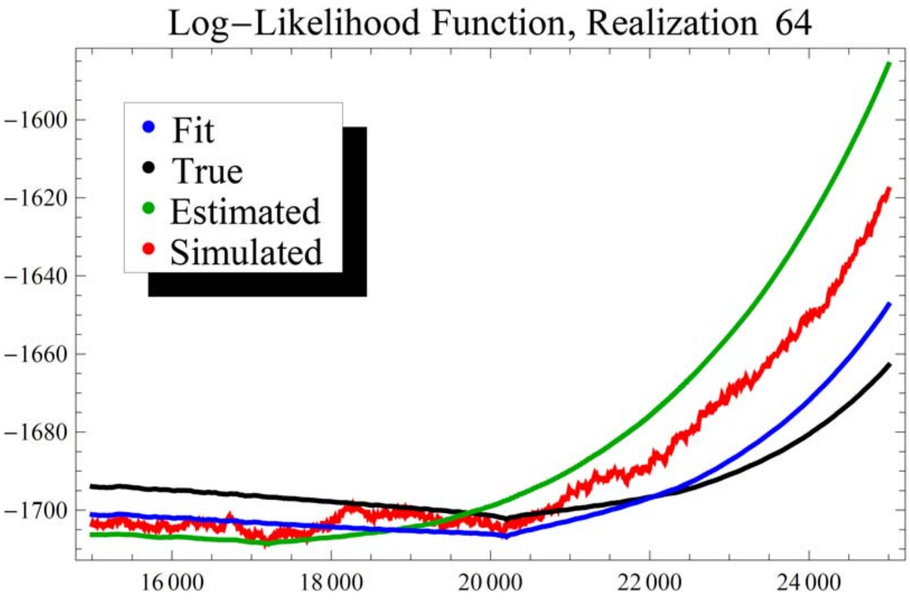

Fig. 24. Log-likelihood functions, as a function of η_1 in km for realization 64, showing hand-fitted as well as estimated and true functions.

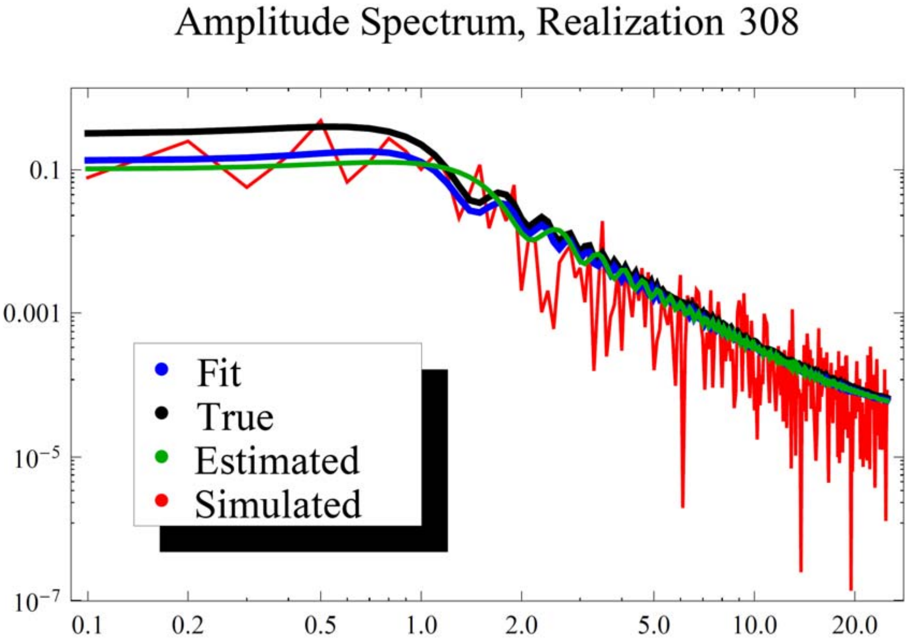

Fig. 25. Amplitude frequency spectrum (in Hz) for realization 308, showing fit ($\eta = 20\,200$, $L = 2.5$ km, and $C_n^2 \Delta\eta = 3.36 \times 10^{-9}$), compared to estimated ($\eta = 22\,550$ km, $L = 5$ km, and ($C_n^2 \Delta\eta = 2.07 \times 10^{-9}$).

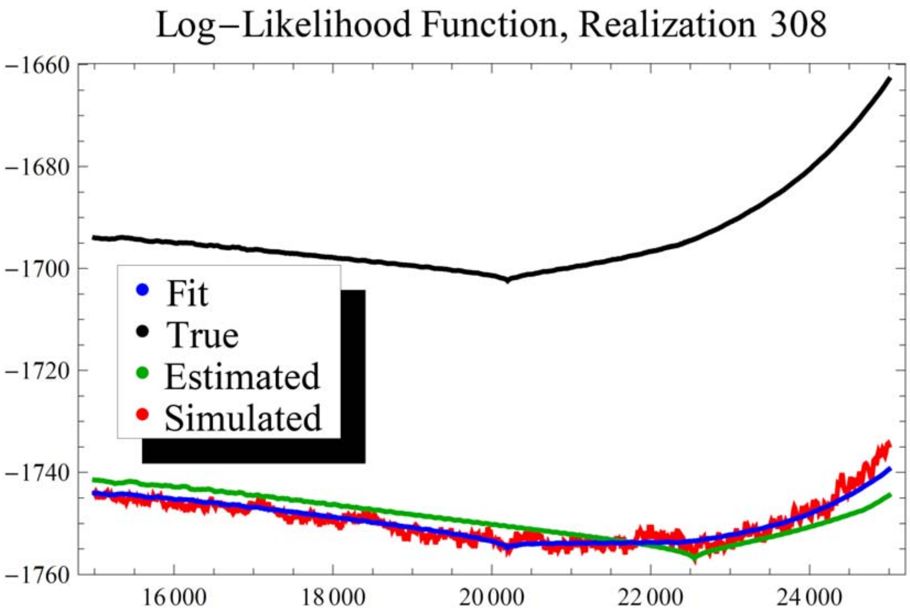

Fig. 26. Log-likelihood function, as a function of η_1 in km, for realization 308 showing results from fit and ML estimation.

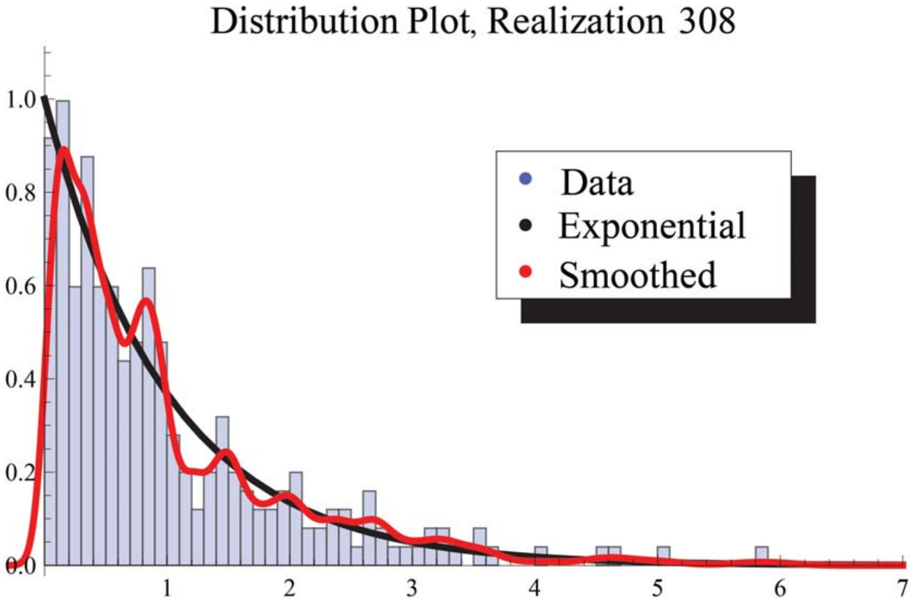

Fig. 27. Distribution of ratios for realization 308.

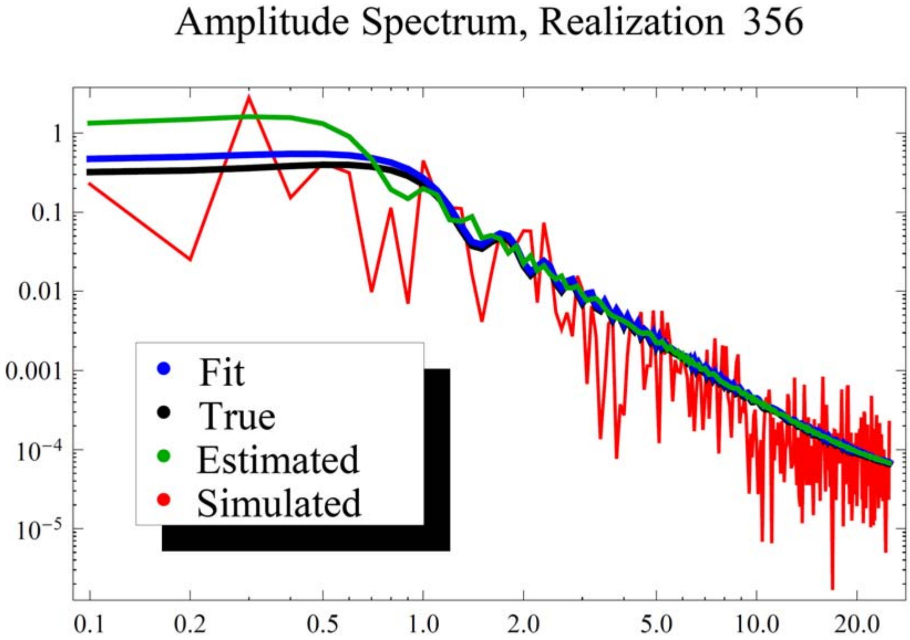

Fig. 28. Amplitude frequency spectrum (in Hz) for realization 356, showing fit ($\eta = 20\,200$, $L = 9$ km, and $C_n^2 \Delta\eta = 4.32 \times 10^{-9}$), compared to estimated ($\eta = 17\,320$, $L = 5$ km, and $C_n^2 \Delta\eta = 9.1 \times 10^{-9}$).

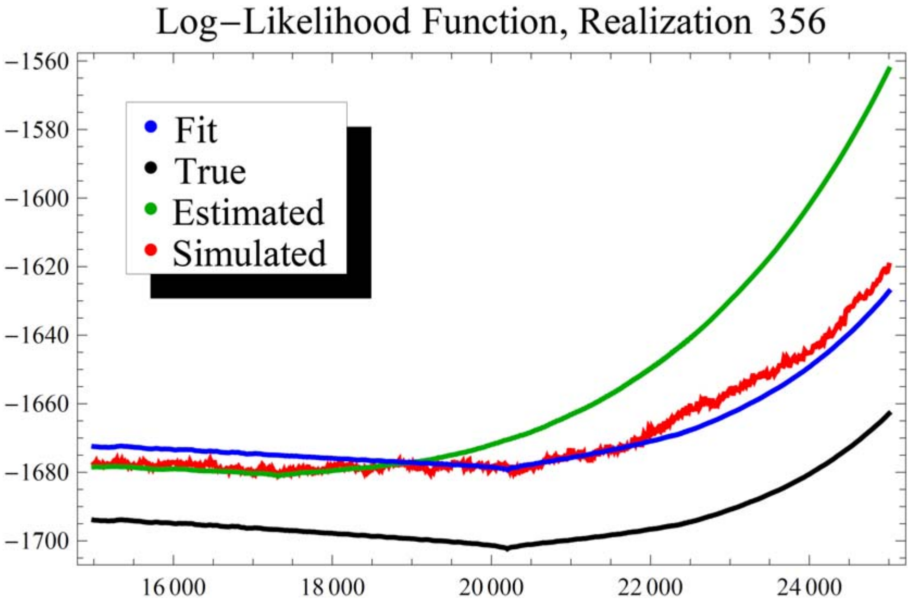

Fig. 29. Log-likelihood functions, as a function of η_1 in km, for the spectra shown in Fig. 28.

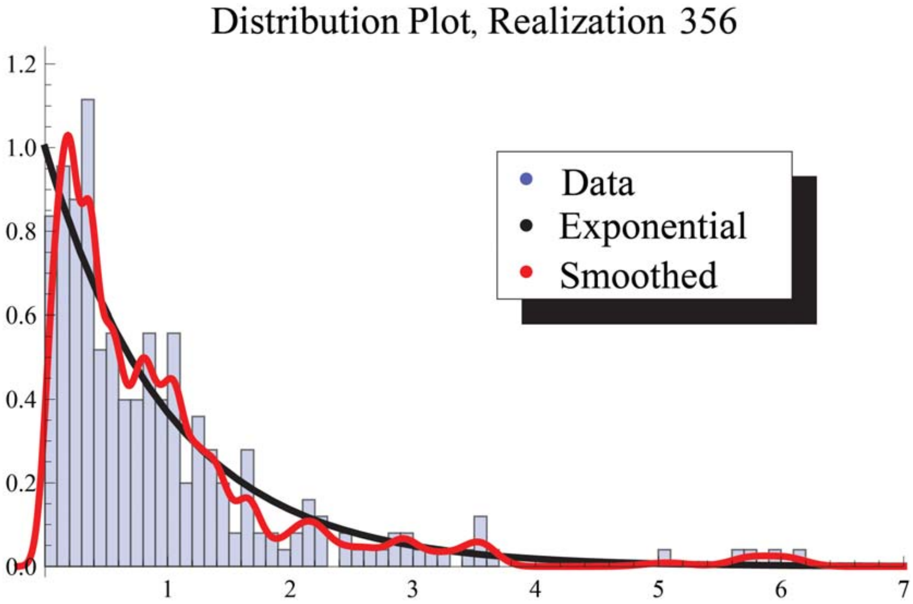

Fig. 30. Distribution of ratios for realization 356 - low p-values.

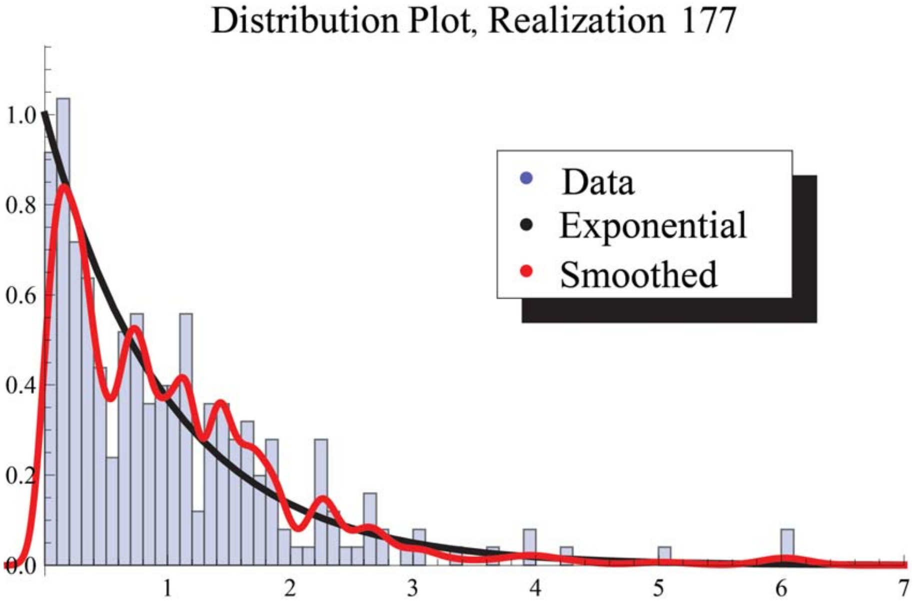

Fig. 31. Distribution of ratios for realization 177 - low p-values.

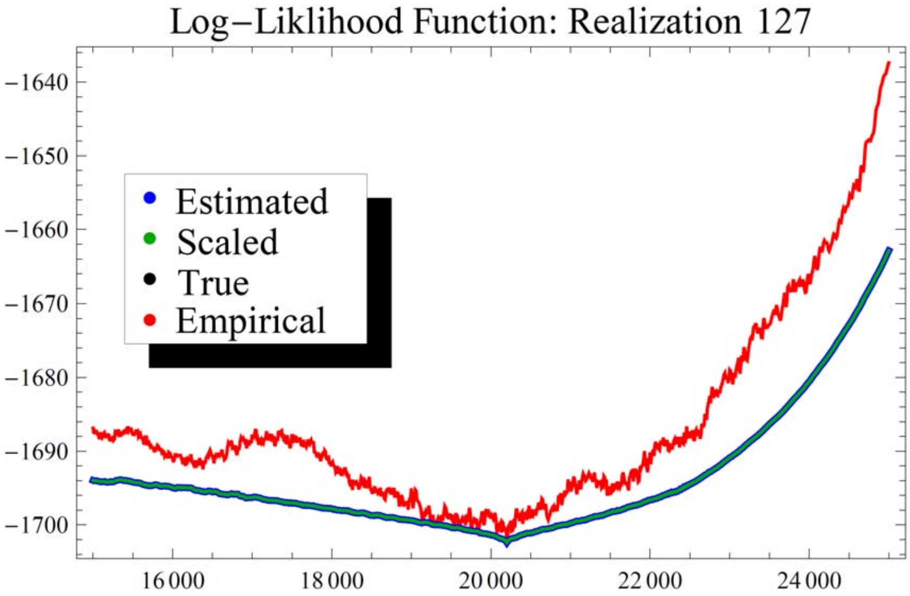

Fig. 32. Log-likelihood functions, as a function of η_1, for realization 127.

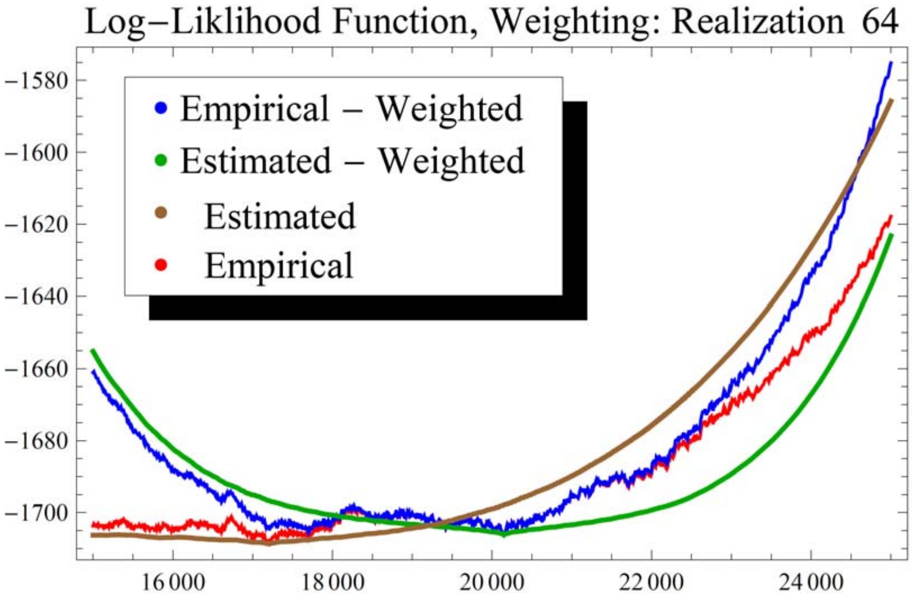

Fig. 33. Log-likelihood functions (as a function of η_1 in km) – empirical and estimated – for the basic and weighted parameter estimation methods. The data are from realization 64.

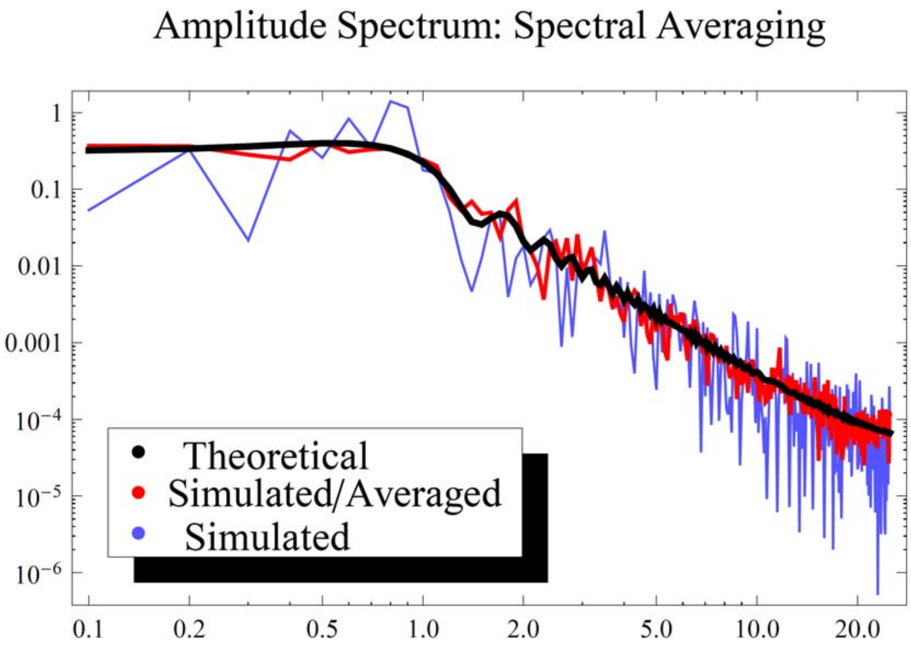

Fig. 34. The effect of spectral averaging on reducing the random errors in the amplitude frequency spectrum. Five realizations were averaged. The "simulated" curve is from realization 127, and is shown merely as a reference.

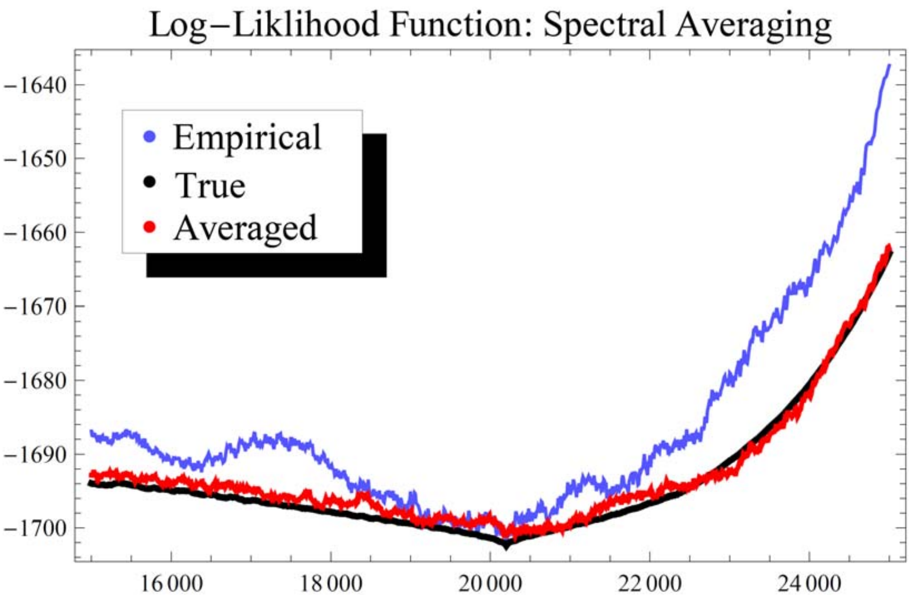

Fig. 35. The effect of spectral averaging on the log-likelihood function, as a function of η_1 in km. The "empirical" curve is from realization 127, and is shown merely as a reference.

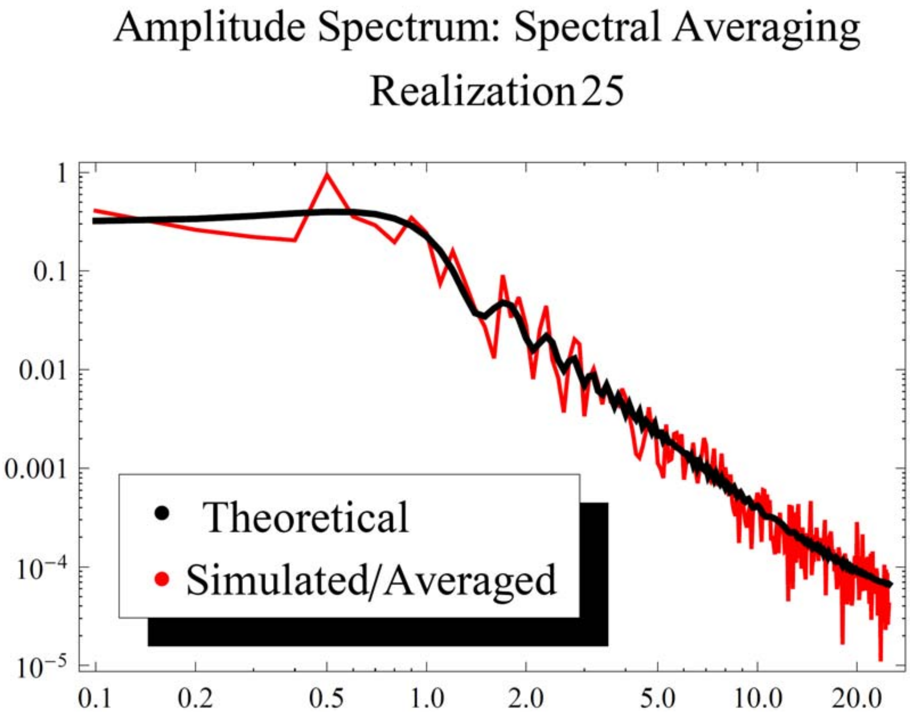

Fig. 36. Averaged and theoretical frequency spectra (in Hz). Five spectra, beginning at realization 25, were averaged.

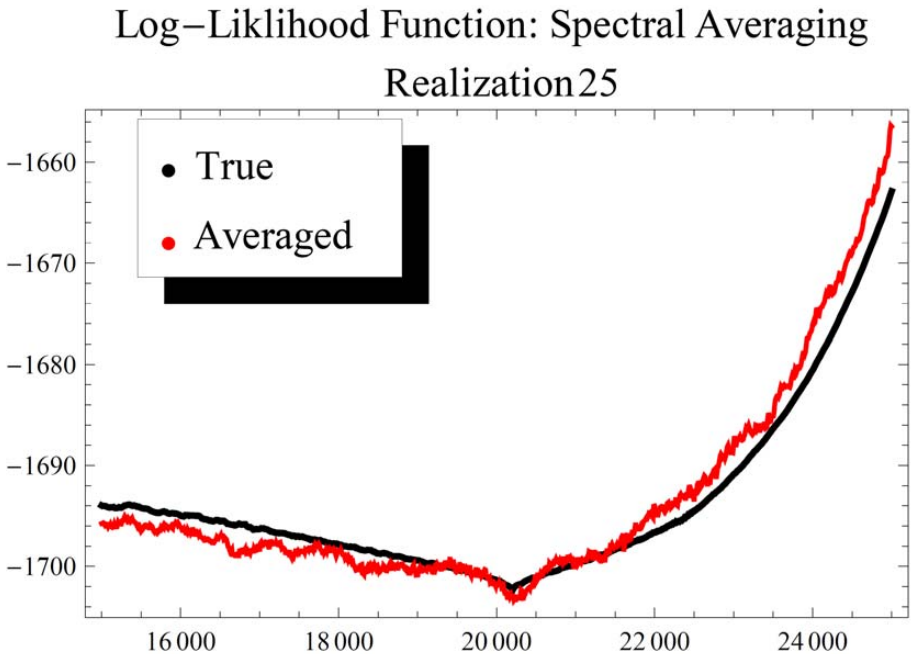

Fig. 37. Log-likelihood function, as a function of η_1 in km, derived from averaged and theoretical amplitude frequency spectra. Five spectra, beginning at realization 25, were averaged.

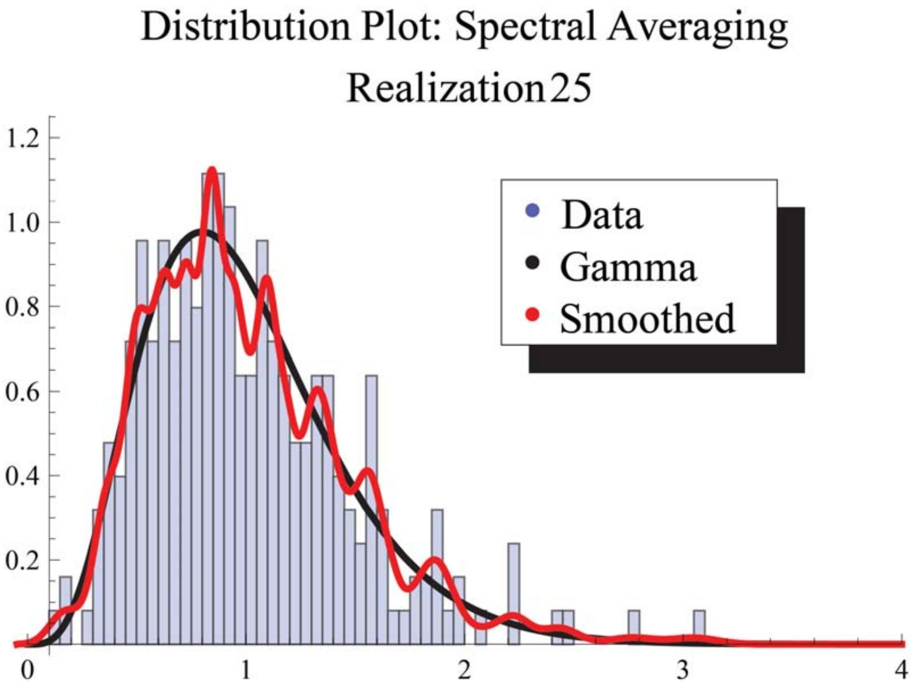

Fig. 38. Distribution of ratios for the five averaged amplitude frequency spectra shown in Fig. 36, above. Note that the theoretical density function is from a gamma distribution.

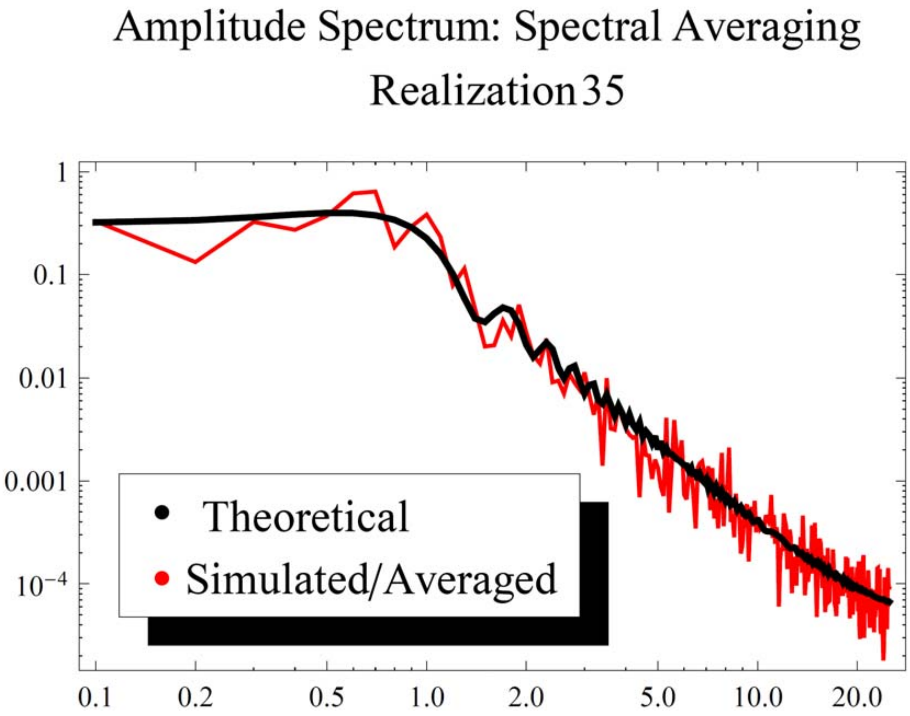

Fig. 39. Averaged and theoretical amplitude frequency spectrum (in Hz). Five spectra, beginning at realization 25, were averaged.

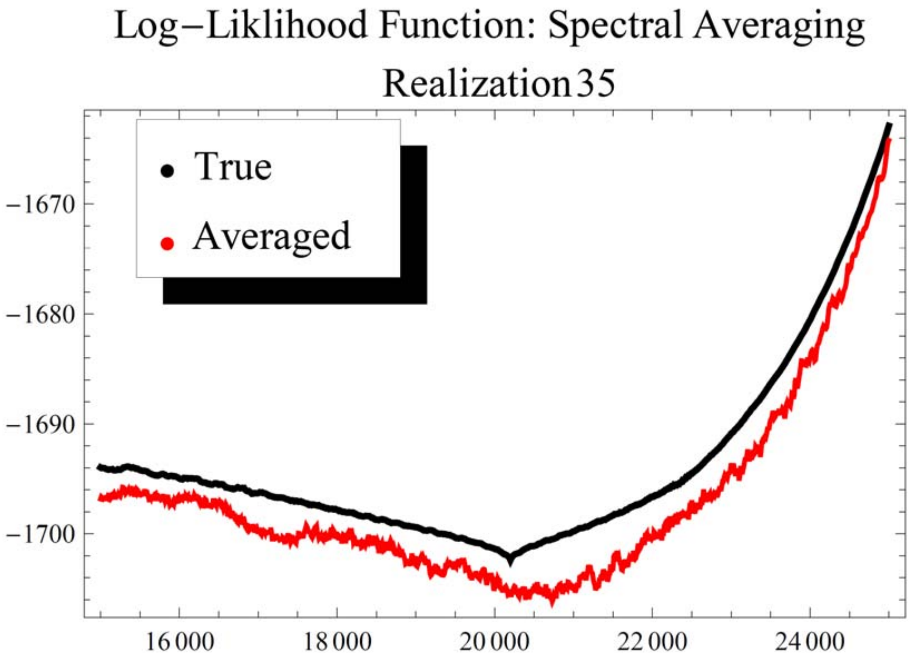

Fig. 40. Log-likelihood function derived from averaged and theoretical spectrum. Five spectra, beginning at realization 35, were averaged.

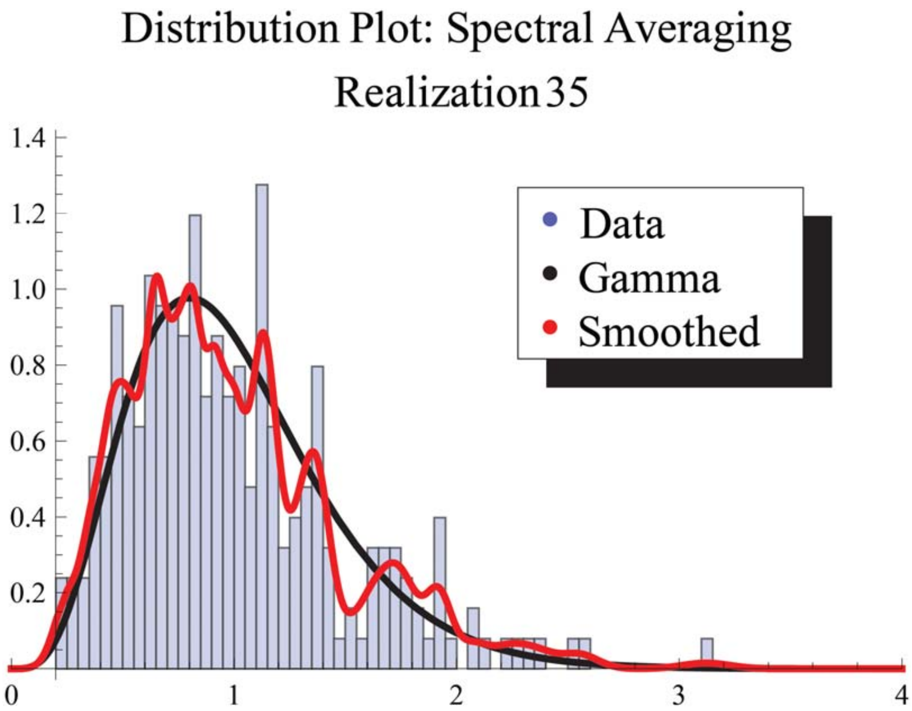

Fig. 41. Distribution of ratios for the five averaged spectra shown in Fig. 39, above. Note that the theoretical density function is from a gamma distribution.

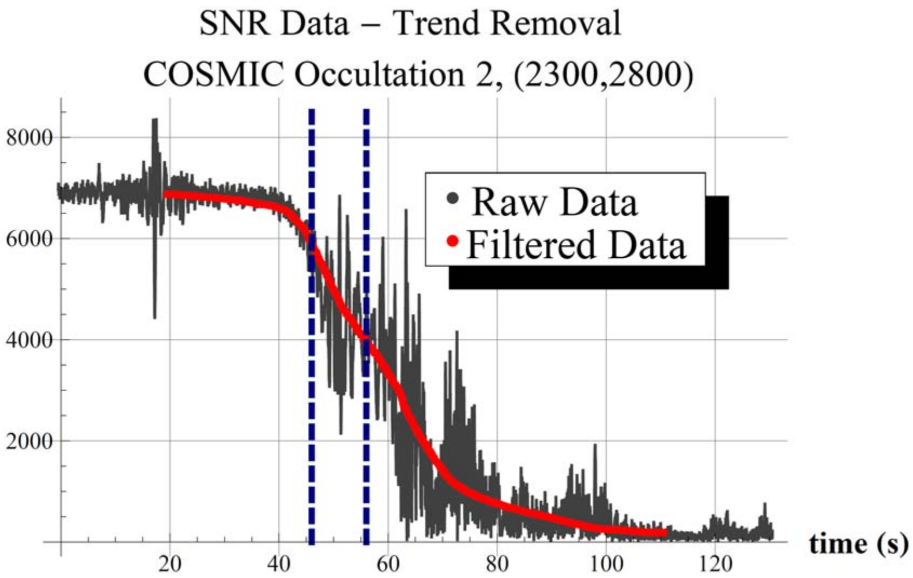

Fig. 42. SNR data for COSMIC occultation number 2 (black). Trend curve is in red and the vertical, dashed blue lines indicate the analysis window.

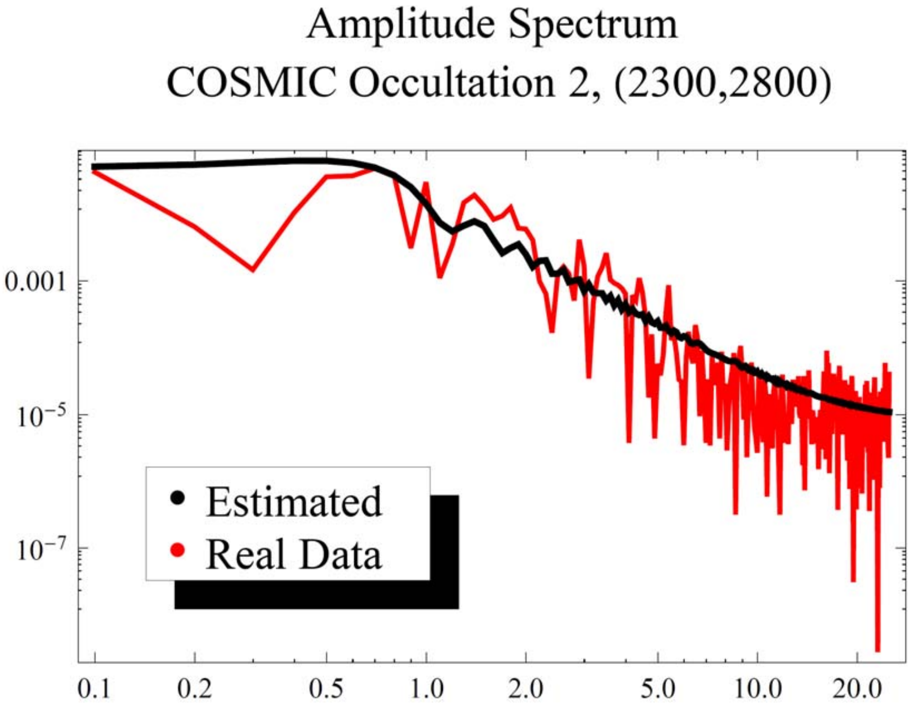

Fig. 43. Amplitude frequency spectrum (in Hz) for occultation 2 (red) and model spectrum using estimated parameters (black).

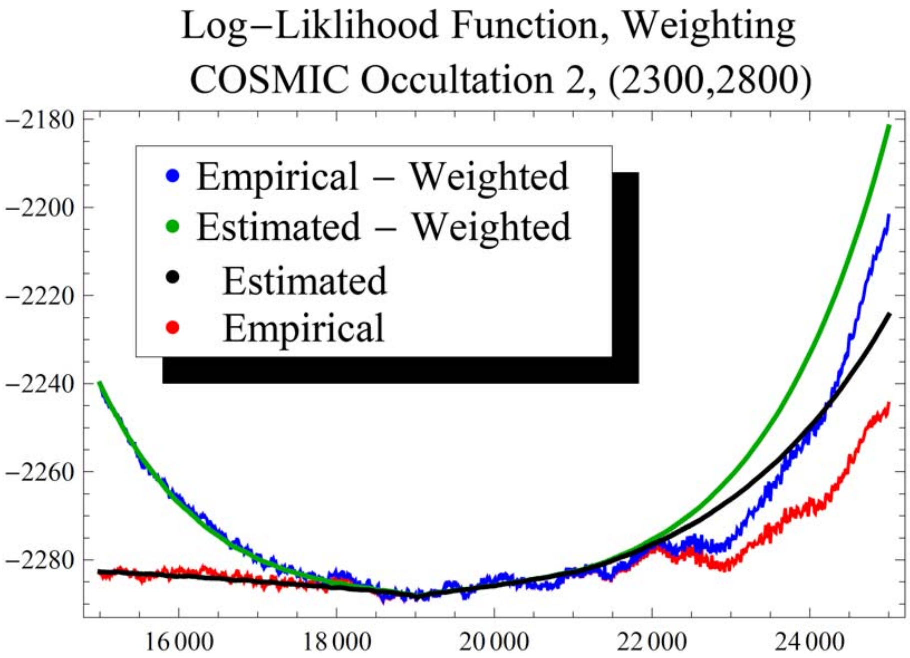

Fig. 44. Weighted and non-weighted likelihood functions, as a function of η_1 in km, from empirical and estimated amplitude frequency spectrum for occultation 2.

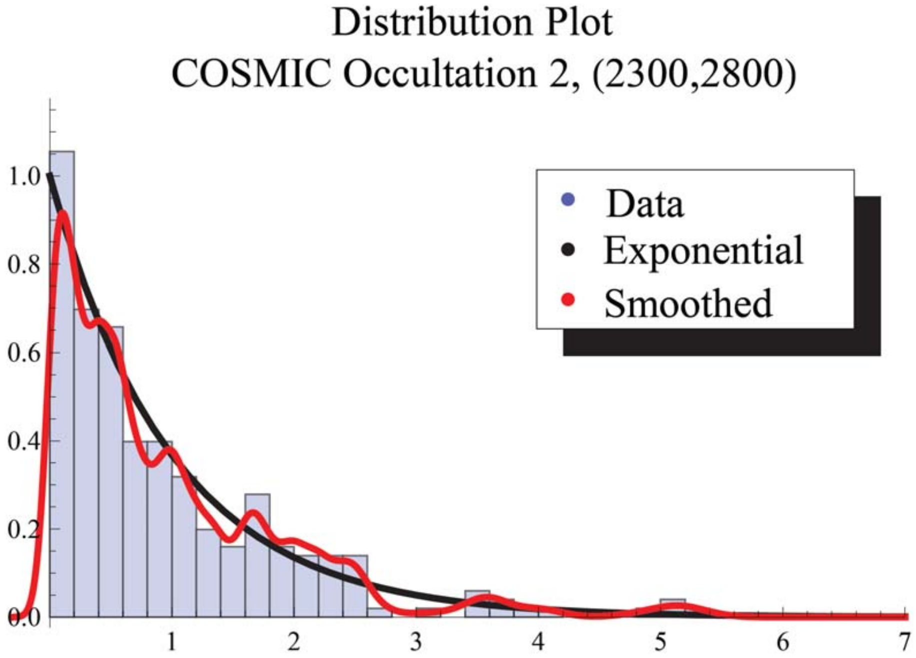

Fig. 45. Distribution of ratios for occultation 2.

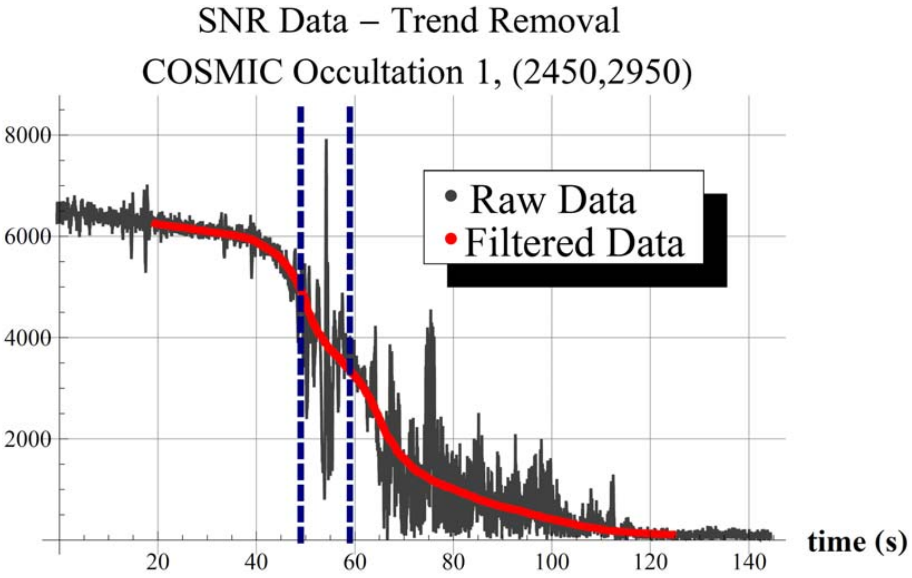

Fig. 46. SNR data for COSMIC occultation number 1 (black). Trend curve is in red and the vertical, dashed blue lines indicate the analysis window.

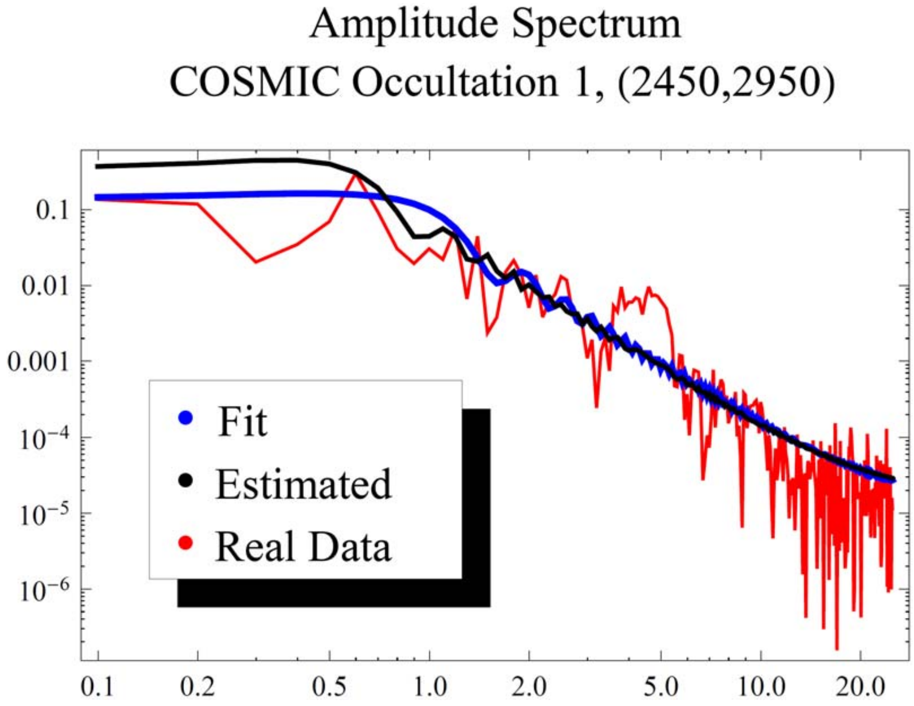

Fig. 47. Amplitude frequency spectrum (in Hz) for occultation 1 (red) and model spectrum using estimated parameters (black) and "by-eye" fitted parameters (blue).

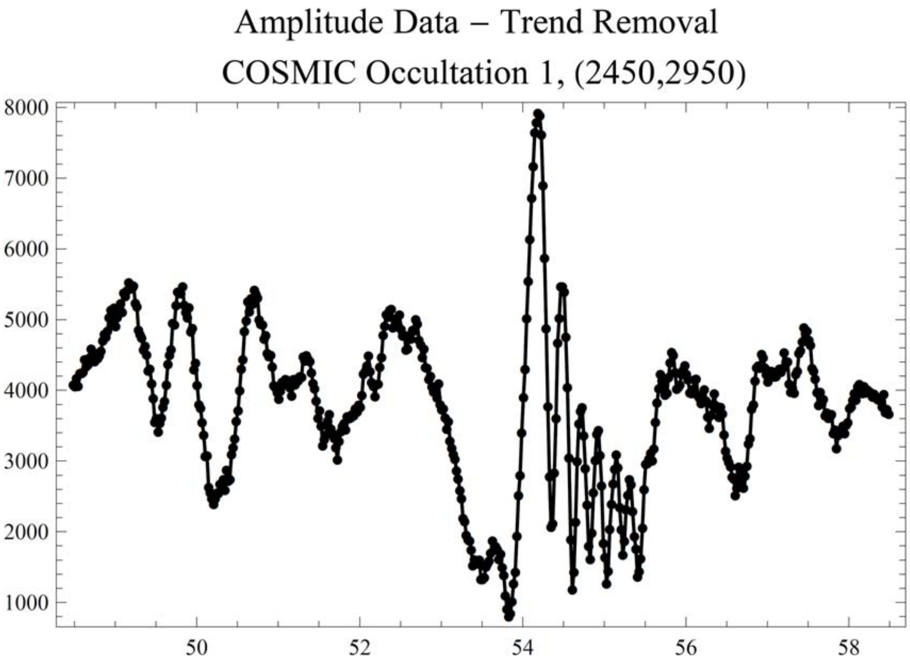

Fig. 48. De-trended SNR time series (in seconds) from the analysis window for occultation 1. (Between the vertical, dashed blue lines in Fig. 46.) Note spike just after 54 s, and oscillations ("ringing") for the subsequent 1.5 s.

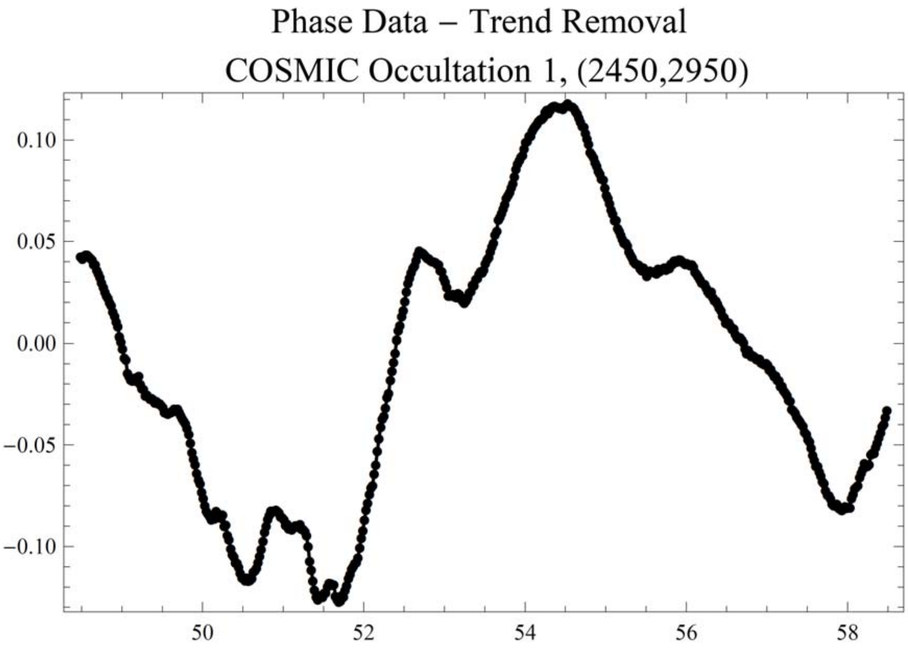

Fig. 49. De-trended phase data (in seconds) over the same time period shown in Fig. 48.

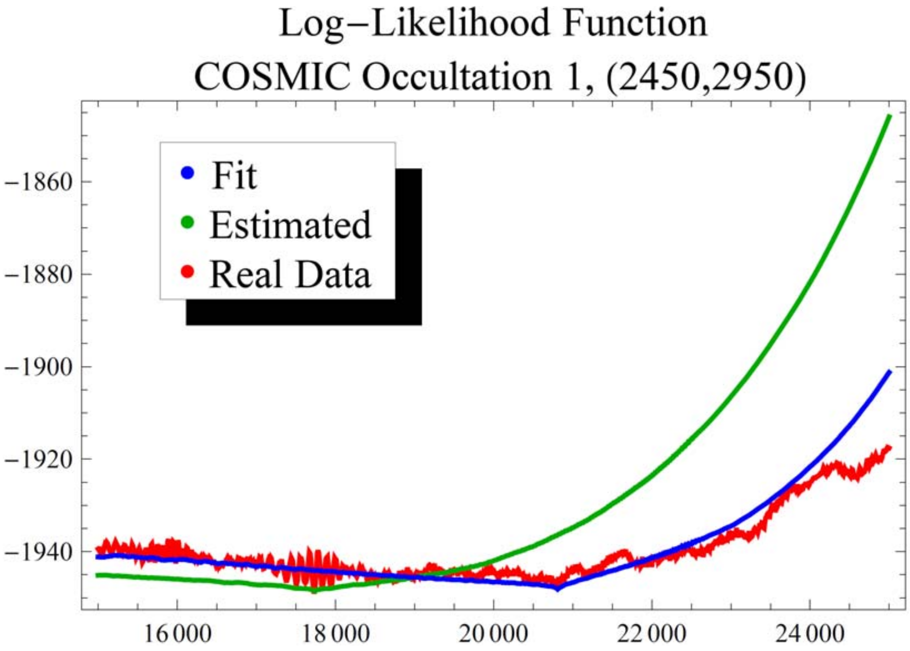

Fig. 50. Log-likelihood functions, as a function of η_1 in km, from empirical, estimated and fitted amplitude frequency spectra for occultation 1.

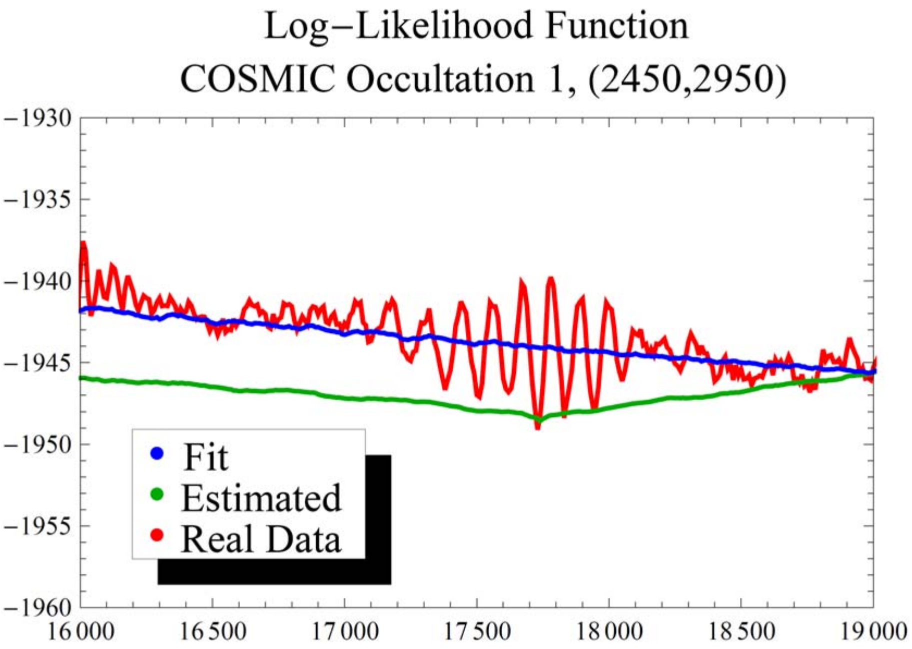

Fig. 51. Blow-up of the log-likelihood functions, as function of η_1 in km, shown in Fig. 50. Oscillations in the empirical curve are due to those seen in the time series (Fig. 48).

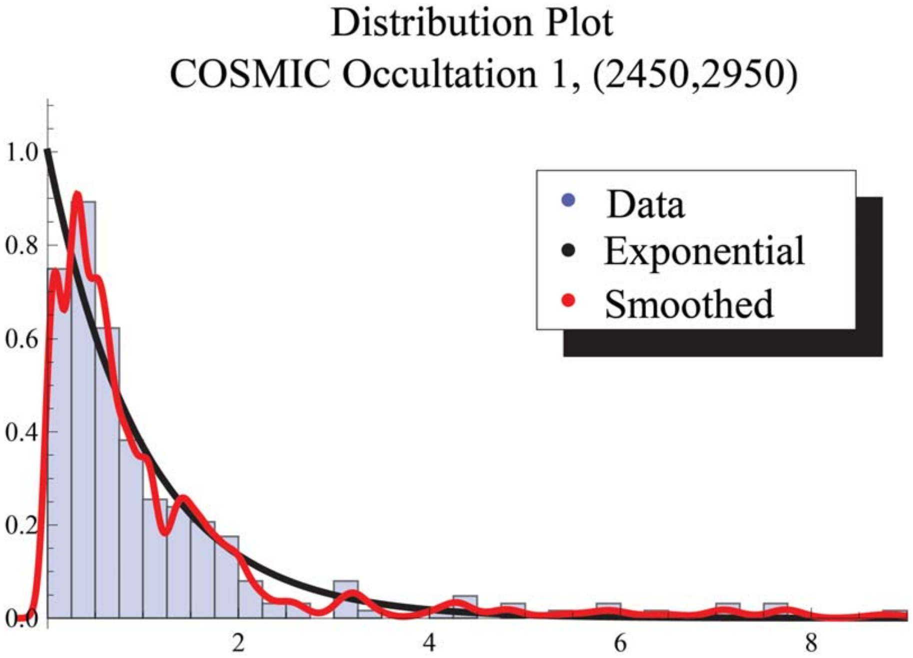

Fig. 52. Distribution of ratios for occultation 1. Note enlarged horizontal scale to accommodate large outliers.

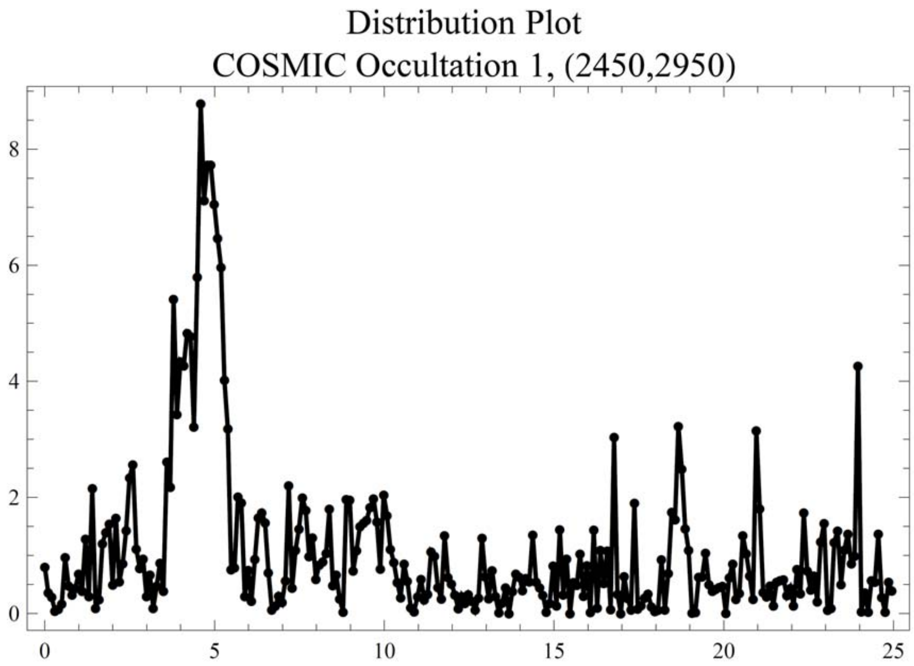

Fig. 53. Ratios as a function of frequency for occultation 1.